UNIVERSIDAD NACIONAL AUTÓNOMA DE MÉXICO
PROGRAMA DE MAESTRÍA Y DOCTORADO EN INGENIERÍA
INGENIERÍA MECÁNICA (TERMOFLUIDOS)

Estudio multifásico de la turbulencia en flujos con superficie libre

TESIS

QUE PARA OPTAR POR EL GRADO DE
DOCTOR EN INGENIERÍA

PRESENTA:
JOSÉ MANUEL CUBOS RAMÍREZ

TUTOR
DR. MARTÍN SALINAS VÁZQUEZ
INSTITUTO DE INGENIERÍA

MIEMBROS DEL COMITÉ TUTOR
DR. WILLIAM VICENTE Y RODRÍGUEZ, INSTITUTO DE INGENIERÍA
DR. RUBÉN ÁVILA RODRÍGUEZ, FACULTAD DE INGENIERÍA

Ciudad Universitaria, Cd. Mx. **mayo 2017**

Abstract

In this study, an efficient three dimensional two phase flow model for simulation of a plunging breaking wave is presented. The method is based in the solution of Navier-Stokes equation for quasi-incompressible flows. The equations in generalized coordinates are solved by extension of the fully explicit MacCormack scheme, second order in time and fourth order in space. The free surface is implicitly captured by the zero level set of a smooth function and by the Ghost Fluid Method to capture accurately shape discontinuities for properties in the vicinity of the interface. Finally, the volume of fluid method is used to ensure mass conservation. Turbulence is described by large eddy simulation, where only the large-scale eddies are solved, while the small scales are modeled by using the selective structure function subgrid-scale model. Boundary shapes are represented through the immersed boundary method on the Cartesian grid. The accuracy of this numerical model is validated by some free surface problems in terms of free surface elevations. Finally a a further study of turbulent structures characteristics during a single plunging dam-breaking wave is performed. Numerical predictions by all cases are in good agreement with experimental data.

Declaration

This dissertation is the result of my own work, except where explicit reference is made to the work of others, and has not been submitted for another qualification to this or any other university.

José M. Cubos

Acknowledgements

Of the many people who deserve thanks, some are particularly prominent, such as my supervisors...

The authors appreciate the financial support provided by Universidad Nacional Autónoma de México, PAPIIT DGAPA- IN106112. Computation was carried out at the Tonatiuh-cluster (Instituto de Ingeniería, UNAM). The authors thanks Fernando Maldonado, Tonatiuh-cluster manager and his team ASUL

Preface

Wave breaking in the surf zone represents one of the most spectacular and extremely complex phenomena we can find in nature. Knowledge of this physical process highly turbulent is essential as it has implications in fundamental fluid mechanics, coastal engineering, oceanography and naval hydrodynamics.

Although considerable progress in theoretical, experimental, and numerical aspects has been made in recent years, some important characteristics of breaking waves have not been investigated in detail. Among them are the complex phenomena of two-phase flows and the turbulence structure especially for three-dimensional flows with complex geometries, which represent a challenges to further computational studies and the need of sophisticated numerical techniques.

The objective of this study is to develop a flexible Large Eddy Simulation numerical model with the potential to adapt over the time with few modifications for carrying out simulations of real-life turbulent free surface flow problems with complex configurations such as breaking wave phenomena. The capabilities of the developed model is verified in terms of efficiency, accuracy and flexibility for exploiting a parallel architecture.

This thesis is organized as follows. A brief introduction describing the wave breaking problem and the state of art of both laboratory and numerical contributions for free surface flows are presented in Chapter 1. A general description of the governing equations, numerical method, solution procedure an the free surface model is presented in Chapter 2. Two test cases to demonstrate the performance and effectiveness of the presented method are presented in Chapter 3. A further study of a single plunging dam-breaking wave dynamics and turbulent characteristics is presented in Chapter 4. Conclusions are discussed in Chapter 5.

Contents

"However far modern science and technics have fallen short of their inherent possibilities, they have taught mankind at least one lesson: Nothing is impossible."

— Lewis Mumford

Chapter 1.

Introduction

1.1. Problem description

As an ocean wave propagates into shallow water depth, a complex highly nonlinear phenomenon begins. During this process; celerity reduces; its wavelength decreases; and its height increase until this reach a critical level and becomes asymmetric, unstable, and finally it breaks. Depending on the characteristics of the incoming wave and beach profile, waves break in a different way [1]. Among the different types of breaking waves, plunging breakers represents one of the most dominant and violent breaking types. Plunging waves are characterized for the formation of a jet at the crest that projects out from the front face and impacts the free surface with a splash below the mean water level. The impact traps air pockets and leads to the generation of turbulence; the plunging jet forms an inner air core or tube, where the trapped air is quickly compressed by the moving wall beneath the crest and sometimes vents through the surface in a sudden spout. The roller interacts with the fluid below it in a complicated way, exchanging energy and momentum in the process. The roller will eventually dissipate and be completely absorbed by the wave.

The characteristics of the complex flow induced by plunging breaking waves and the presence of a two-phase turbulent flow beneath the surface just after the breaking event has meaning a challenge and a topic of mayor interest for many researchers in recent years [2], [3], [4]. Because the irregular nature of a breaking wave event, it is difficult to conduct experiments in the field, so most of studies dedicated to understand the physical processes involve in breaking wave events are based in laboratory experiments and numerical simulations. Though experimental research has played an important role

improving the understanding of breaking waves hydrodynamics and generating significant physical insights and reliable results useful for calibrating and validation of computational fluid dynamics models. These studies has focused in the analysis of the hydrodynamic of general flow patterns like the evolution of the free surface deformation and wave kinematics. In most studies, especially for plunging wave breaking, detailed description of processes, such as jet overturning, splash-up, air entrainment, instabilities and turbulence characteristics are not included in the analysis.

On the other hand, with improved computer capabilities the use of numerical models based in the solution of the fundamental equations of fluid mechanics to study breaking waves phenomena is a common practice in modern environmental engineering. This approach complements experimental and theoretical studies by providing an alternative cost effective means of simulating real flows situations. In coastal engineering field it methodology allows a detailed description of the complex three-dimensional flow patterns generated by breaking waves under conditions sometimes unavailable experimentally. Most of existing numerical models for breaking waves are based on Direct numerical Simulation (DNS), Large Eddy Simulation (LES) and RANS-based models. With DNS every fluctuating motion in the flow is solved without any modeling simplification or assumptions, but considering the computational requirements particularly in three dimensions problems DNS is not a practical alternative and results prohibitive at high spatial resolutions. RANS models represents the most widely used approach and an attractive alternative in terms of computational cost, however they have considerable limitations in modeling turbulent characteristics and vortical patters on aerated regions since all turbulent length scales are modeled [5], [6], [7]. With LES the larger turbulent features are simulated by solving the flow equations, and the small scale turbulence that is not resolved by the flow model is represented by a sub-grid model. This technique lies between DNS and RANS in term of computational demands while offers a detailed description of turbulent characteristics such as coherent vortical structures and motions of intermittent nature. LES methodology have showed very promising results, for three-dimensional breaking wave simulations, focussing on air entrainment phenomenon and a correct description of the free surface [8]; [9]; [10]. However, a few studies focused the attention to discuss the turbulent flow structure subsequent to wave breaking.

1.2. Experimental and numerical contributions review

The wave-breaking-induced turbulence characteristics have been a subject of considerable research in recent years. Both experimental and numerical studies, have significantly improved the understanding and knowledge of the complex physical processes during wave breaking, such as free surface evolution, air entrainment, and turbulence especially for three dimensional flows.

Pioneering laboratory studies revealed that the flow under breaking waves is characterized by large-scale, organized flow structures. [11] studied the structure of the turbulence flow field under periodic spilling breaking waves. In their work, in addition to two-dimensional structures around the wave crest, three-dimensional large-scale vortex structures behind the wave crest, which stretches obliquely downwards were identify. This structures called "obliquely descending eddies" penetrate into the water column interacting with the bed. An extensive study on turbulence under spilling and plunging breakers is given by [12], [13] founding that the turbulence dynamics are strongly influenced by the breaker type. Their results showed that the mean flow transports the turbulent kinetic energy seaward under a spilling breaker and landward under a plunging breaker with a dissipation rate slower in the former and large-scale motions in the later. Recently, laboratory observations have revealed the existence of some interesting features of organized flow structures called called downburst under a solitary wave [14]. A downburst is a vortex with axis of rotation in the vertical direction formed when the water spilling down the front face of the breaking wave produces a turbulent, aerated water mass. The collapse of the subsequent splash-up in reverse breaking causes this aerated water mass to descend toward the bottom producing even more sediment transport than obliquely descending vortices.

More recently, motivated by an increasing computational development, several studies have demonstrated that turbulent structures under breaking waves can be accurately captured and described by a large eddy simulation approach since provide a sufficient amount of high-resolution information for an adequate description of the turbulence and allows to capture coherent vortices structures under breaking waves. Most of the numerical works have been dedicated to reproducing the three dimensional coherent vortices founded experimentally [15]; [16]; [17]. These studies have provided a detailed and accurately description for both the free surface and the generation and evolution of the turbulent structures. However, only a few studies have focussed on the instantaneous small-scale structures and other importante features during for a plunging breaker such

the scars and instabilities on the plunging jet surface just before the impact and the aerated filaments around the air tube trapped during the splash up process.

The above studies have included both periodic and solitary waves. The wave generation method have been based on inflow boundary condition, applying a velocity profile obtained from an analytical solution and through a internal wave generation method in which a mass source function computed according to a prescribed free surface profile is introduced in a certain region inside the computational domain such that it produces the same physical effect of the desired wave. An alternative novel method for reproducing a wave is to generate a large-scale bore through dam-break on a wet bed. In this wave generation method proposed by [18]: [19]; [20], a deep reservoir of liquid is separated from a shallow body of water by a gate that can be removed at high speed. The sudden opening of the gate produces a bore that subsequent collapse in a plunger breaking wave form. The surface, vorticity and turbulence are completely controlled by relative collapse height with respective to water depth.

The main advantage behind studying a single breaking wave is that the wave breaking process and the generation and evolution of the associated three-dimensional vortex structures can be investigated separately from the effect of returning undertow flow and the residual turbulence induced from previously broken waves in the case of periodic waves. Further, a single breaking wave results less computationally time comparing to periodic wave conditions and hence it allows us to use higher numerical resolution.

1.3. Free surface modeling methods review

In view of the complexities of moving and deforming surfaces, nonlinear effects, large range of length scales and time scales, high turbulence, among other causes, accurate description of physical processes involving a free surface represents still a challenge, even for the most sophisticated models. Free surface represents a dynamic boundary, whose position and shape change in response to the interaction between the phases present; therefore, use of special techniques is needed to define the location and movement of the interface. Owing to the complexity of free surface flows, a large number of modeling methods for interface simulations have been developed. These approaches can be divided into two great classes: moving-grid methods (Lagrangian approach) and fixed-grid methods (Eulerian approach). In addition to these methods, there are special cases, such as particle methods, in which grids are not needed.

In Lagrangian description, coordinate system follows the movement of the fluid particles. The interface is a boundary between two subdomains of the grid, so the free surface is sharply defined. Although it seems the most natural way to simulate free surface flows, this method is restricted to well-defined simple surface topologies, because the grid has to be re-meshed or refined when the interface undergoes large deformations and topology changes. Meanwhile, in Eulerian, the mesh is fixed in the space. This method introduces a new variable in the model to track the presence or not of one of the two phases in the whole domain. Eulerian methods are the most used ones, since they permit to take into account large topology changes and discontinuities. Methods that fall into this category include the volume-of-fluid (VOF) method introduced by [21] and the level-set (LS) method introduced by [22]. In the former, a steep function, transported by the fluid flow, is defined in the whole computational domain. This function, which represents the fraction of the volume, is set to unity everywhere in one phase and zero in the other phase. In those regions where both phases are presented, free surface is captured through a interface reconstruction procedure. The mayor advantage of this method is the mass conserving properties. Nonetheless, the interface reconstruction is a laborious computational task. In addition, modeling errors stem from the difficulties to control the interface thickness, due to numerical diffusion. In the LS approach, the interface is simulated by the evolution of the zero level of a time-dependent smooth function transported by the fluid flow. This approach allows the simulation of complex surface evolution including topological merging and breaking; moreover, the computation of geometrical quantities like the normal and curvature of the interface are easily performed. The LS approach provides an exact representation of the interface, but it is by definition a not mass conserving method.

In the context of the LS method, several approaches have been developed in pursuance of maintaining the interface sharp and to improve mass conservation properties. [23] , [24] , [25] and [26] improve conservation properties by replacing the usual signed distance function of the original LS approach by a hyperbolic tangent function. This proposed function is transported and reinitialized using conservative equations reducing mass conservation errors while retaining the simplicity of the classic method even for complex problems. Another strategy is to implement the adaptive mesh refinement (AMR) technique. This technique was introduced by [27] and later extended for the two-phase incompressible flow by [28]. In this approach, multiple component grids of different resolutions are used. In a region of the flow when more detail is required, a refined grid is placed. This approach has been used in combination with LS method by [29] and [30] not only to improve mass conservation, but also to preserve interfacial topologies.

Also [31] used this technique in combination with LS method to simulate moving solid boundaries. Finally, methods that combine two different methods and takes advantages of the strengths of each of the two approaches have received considerable attention in recent years. It can be found that LS and VOF methods have the complementary advantages and disadvantages, so it is a natural trend to develop a method combining these approaches. The basic idea behind combining VOF method and LS method is to get the best from both VOF method (mass conservation properties) and LS method (easy computation of geometric properties of the interface and interface sharpness). Examples of these methods are the Coupled Level Set Volume Of Fluid (CLSVOF) method of [32], the Coupled Volume of Fluid and level Set (VOSET) method of [33], the hybrid Level set/Volume of Fluid (LS/VOF) method of [34], and the Mass Conserving Level Set (MCLS) method of [35]. These methods have been extensively tested and validated. Results presented in [36], [37], [38], [39], [40], [41] have shown interfacial geometric properties more accurately and mass conservation improvement compared to standard LS and VOF methods.

The level set function ϕ is defined as a signed distance function. However, after the advection procedure this initial condition is not preserved and a reinitialization treatment is always necessary in order to overcome some numerical instabilities and maintain a numerically well-defined interface and maintain an stable interface evolution. The two most popular approaches among them are the Fast Marching Method (FMM) [42] and the Partial Difference Equation (PDE) based Method [43]. The FMM represents the most efficient reinitialization method. However, the algorithm is inherently sequential due to causal relationship between grid points and hence not straightforward to parallelize. PDE-based method represents a simple and yet efficient alternative. In this method, the values in all grid points are updated simultaneously, therefore, the algorithm is well suited to parallel computing environments. Additionally, this method offer the advantage of flexibility to use a wide range of well documented numerical techniques as well the use higher-order schemes for time and space discretization. In this work, the PDE-based method approach [44] is adopted

In this work, the approach proposed by [35] is adopted. The MCLS method is a hybrid method, based in an explicit relation between the LS function and the VOF function to find a mass conserving correction to the LS function. The locally linearized LS function and the VOF function are linked through an algebraic relation, based on a parameterized geometric construction of the interface. The method takes full advantage of all additional information provided by the Level Set function, rather than coupling LS method with VOF method. The VOF function is used as an auxiliary variable to

conserve mass, without applying the difficult interface reconstruction which makes the VOF method so elaborate and computationally expensive. However, the classic implicit representation of the LS method used in [35] tracks all the LS functions throughout the entire computational domain, even though interest is really confined only to the zero LS itself corresponding to the interface. This consideration results computationally expensive. [45] introduced the idea of the narrow band approach, also called Local LS method to limits labor to a thin region around the zero LS. The savings of the use of local LS methods has been reported by [44], therefore this modified approach of the LS method is adopted in this work.

On the other hand, in order to improve the accuracy and handling large gradients and material discontinuities associated with two-phase flows, the Ghost Fluid Method (GFM) of [46] is adopted. This technique based in the approach introduced by [47] provides a way of dealing problems involving large density ratio i.e. when one fluid is too stiff compared with the other, such as, air/water interface. The GFM consists in creating an artificial fluid also call ghost fluid which implicitly induces the proper conditions at the interface. In the ghost fluid regions, discontinuous variables across a fluid interface are given using a one-sided extrapolation and continuous variables are copied from the real fluid on a node-by-node basis. Finally, high-order schemes such as the Weighted Essentially non Oscillatory (WENO) scheme of [48] for space discretization and the third order TVD-RK of [49] for time discretization are used. These schemes are capable of handling large gradients and discontinuities very accurately.

1.4. Scope

In this thesis, an efficient level-set two-phase flow model for the simulation of problems with a large density ratio and complicated interface interactions applied to highly turbulent water-air problems is introduced. Two sets of the flow equations are solved simultaneously, one for each fluid. Both the liquid and gas phases are assumed to be governed by Navier-Stokes equations and approximated to incompressible state through an artificial state equation. The VOF function is computed, so that mass conservation issues of the LS method can be overcome. LS function is only solved in a narrow band across the interface. This approach reduces considerably the computational time, making the method more efficient. Finally, to assure a sharp and correct evolution of the interface, higher order schemes are used for both spacial and temporal discretization. The capability, accuracy

and performance of the presented numerical model is evaluated and validated by carrying out some benchmark numerical simulations. The code has been parallelized using message passing directives (OpenMP). The main advantages of OpenMP. The parallel code which was written in FORTRAN-90 has been successfully tested. The CPU time quantities show that the parallel code achieves reasonably good computational efficiency for fine grid sizes that are relevant for the detail study of relatively high Reynolds number flows, reducing the runtime by a factor of 2.5 with respect to the serial code.

Chapter 2.

Numerical model

In this work, a complex physical phenomena involving large sizes of numerical domains, with both small scales of turbulence and free surface deformations such as breaking waves, is described by the Navier-Stokes equations coupled with mathematical treatments for the free surface and turbulence descriptions. The governing equations are based in a quasi-incompressible formulation. The numerical model is able for the simulation of problems with a highly dynamic interface between air and water, with complicated interface interactions including: wave propagation, wave shoaling and wave breaking. In the numerical method, two sets of the flow equations are solved simultaneously, one for each fluid. The consideration of include the effects of air movement means that the simulations are closer to the realistic situation and this leads to an improve in accuracy compared with one-phase models. The free surface model is based on the level set formulation in which the interface between two immiscible fluids, e.g., air and water, is represented by the zero level set.

The full details of the numerical model may be founded in Appendix A. Here, only a partial description and necessary concepts of the model is presented.

2.0.1. Compressible Navier-Stokes equations

In a Cartesian frame of reference, the two-phase Navier-Stokes equations can be written in the so-called fast conservation form of [50]:

$$\frac{\partial U}{\partial t} + \frac{\partial F_i}{\partial x_i} = \mathbf{S_F} \tag{2.1}$$

where U is the four component vector defined by:

$$U = (\rho_\lambda, \rho_\lambda u_1, \rho_\lambda u_2, \rho_\lambda u_3) \tag{2.2}$$

Here $u = (u_1, u_2, u_3)$ is the velocity vector and ρ is the density. Equation (A.1) represents the evolution of density (continuity equation) and momentum equation.

F_i are the fluxes where $\forall_i \in \{1, 2, 3\}$, and for a Newtonian fluid are given by

$$F_i = \begin{pmatrix} \rho_\lambda u_i \\ \rho_\lambda u_i u_1 + p\delta_{i1} - 2\mu_\lambda S_{i1} \\ \rho_\lambda u_i u_2 + p\delta_{i2} - 2\mu_\lambda S_{i2} \\ \rho_\lambda u_i u_3 + p\delta_{i3} - 2\mu_\lambda S_{i3} \end{pmatrix} \tag{2.3}$$

Finally, the term $\mathbf{S_F}$ corresponds to the source terms, than represent gravity effect. The subscripts λ in Equation (A.3) denote two different material properties, the liquid and the gas phase, respectively, δ_{ij} is the Kronecker delta and S_{ij} is the deviatonic part of deformation tensor, written as:

$$S_{ij} = \frac{1}{2}\left(\frac{\partial u_i}{\partial x_j} + \frac{\partial u_j}{\partial x_i} - \frac{2}{3}(\nabla \cdot u)\delta_{ij}\right) \tag{2.4}$$

2.0.2. Quasi incompressibility approximation

In various numerical schemes for incompressible flow, the pressure is often obtained by solving a Poisson equation. This is frequently the most costly step, which requires additional computations at each time step. A technique to overcome this difficulty is the artificial compressibility (AC) method proposed by [51]. The AC method considers that every theoretically incompressible fluid is actually compressible. The main idea of [51] concept is to add a time derivative of pressure into the continuity equation. This provides a direct coupling between pressure and flow velocity, thus avoiding the need to solve the elliptic Poisson equation. The AC has recently been used along with the LS method in

studying moving interface problems. [52] have extended the AC method for the simulation of incompressible multiphase flows coupling the pseudo-compressibility method and the LS method. The approximation adopted in this work is, in concept, very similar to the artificial compressibility (AC) method of [51] and the pseudo-compressibility method of [52]. The fully compressible continuity and momentum equations are used, but with an isothermal equation of state. This choice allows us to bypass the Poisson equation.

Incompressible flow is approximated by replacing the pressure in the compressible Navier-Stokes equation according with the equation of state $p = c^2\rho$ for an artificial incompressible fluid proposed by [53] and [54] where c is the speed of sound in the medium. As long as the flows are limited to low Mach number, and the conditions are almost isothermal, the solution to this set of equations should approximate the incompressible limit. The sound speed must be chosen carefully to ensure an efficient an accurate solution of a given problem. The value of c must be large enough that the behavior of the corresponding quasi-incompressible fluid is sufficiently close to that of the real fluid, but it should not be so large to make the time step prohibitively small. According to [55] the Mach number, obtained by the reference velocity and the sound speed, should be 0.1 or less.

2.0.3. Equations in generalized coordinates

Although a Cartesian grid is preferred due to the simplicity and efficiency, in Large Eddy Simulation (LES) methodology the generation of a high-quality resolution in the normal near-wall region is a requirement. In this sense, the use of Cartesian grids can result in a high computational inefficiency as the refinement is extended to regions of the flow in which it is not needed, or even to solid regions. The present model has been developed for use in a generalized curvilinear system allowing a wide range of complex geometries to be modeled efficiently on structured grids.

The system in generalized coordinates was solved by means of an extension of the fully explicit McCormack scheme, being second order in time and fourth order in space, as devised by [56]. The explicit MacCormack scheme is essentially a predictor-corrector scheme.

2.0.4. Large eddy simulation

The selection between the large and small scales, is the basic idea of LES. The contribution of the large, energy-carrying structures is computed exactly (completely solved), and the effect of the smallest scales of turbulence is modeled. The justification of such a filtering technique is based in the assumption that large scales contain most of the energy varying from flow to flow, while small eddies are believed to be more universal and less dependent of the main flow.

The separation between the resolved and the modeled scales is mathematically formalized by applying a convolution filter to the Navier-Stokes equations, which introduces the notion of cut-off length. LES should then be an efficient method to overcome the limitations of both DNS and RANS methods.

The two scales categories are subjected to the determination of a reference length, the cut-off length. The large scales, or resolved scales are greater than the cut-off length. The small scales, or sub-grid scales, are taken into account through a subgrid-scale model. In this study, the Selective Structure Function (SSF) model reported by [57] is used. This model allows good results to be obtained for various incompressible and compressible turbulent flows. [58]

2.0.5. Boundary immersed method

Among other things, this work is motivated by the need to develop a method for solving the Navier-Stokes equations that facilitates the implementation of boundary conditions in flows with complex and moving immersed boundaries. The use of immersed boundary method on a Curvilinear grid can improve efficiency by generating grid lines almost parallel to the solid surfaces. This ensures an adequate resolution of the boundary layers. This advantage is particularly beneficial in simulations of turbulent flows with complex geometries [50], [59]

2.0.6. Level-Set methodology

The Level set (LS) method is a simple and versatile method for modeling the evolution of a dynamic interface.This method introduced by [22] is based on the use of a smooth function to describe the interface between two phases. The idea is to represent the

interface implicitly by the zero level set of a level set function, with the corresponding motion of the interface governed by a corresponding PDE.

To implicitly represent the discontinuity, a level set function ϕ is introduced. The level set function at any given point is taken as the signed normal distance from the interface with positive on the liquid phase (i.e. $\phi > 0$), and negative on the gas phase (i.e. $\phi < 0$). Therefore, the interface is implicitly defined as the zero level set of the level set function.

2.0.7. Reinitialization

The level set function ϕ is defined as a signed distance function. However, as the flow field evolves, high velocity gradients can produce wide spreading and/or stretching of the LS function, so this initial condition is not preserved and a reinitialization treatment is always necessary in order to avoid some numerical instabilities and maintain a numerically well-defined interface and a stable interface evolution.

In this work the PDE-based reinitialization approach of [44] is adopted. PDE-based method represents a simple and yet efficient alternative. In this method, the values in all grid points are updated simultaneously, therefore, the algorithm is well suited to parallel computing environments as OpenMP. Additionally, this method offer the advantage of flexibility to use a wide range of well documented numerical techniques as well the use higher-order schemes for time and space discretization.

The reinitialization consists in replace the $\phi(t, x)$ by another function $d(x)$ (Distance function that just is function of the space) that has the same zero level, but $\mid \nabla d(x) \mid = 1$. As well as to the LS equation, Eq. A.22 is discretized using the fifth order WENO scheme in space and third order TVD-RK in time. It is important to use higher-order numerical schemes to minimize numerical errors. It is not necessary to perform reinitialization at every time step. In this work we performed it every 10 to 20 time steps.

2.0.8. Ghost Fluid Method

An accurate treatment of material discontinuities across the interface can be obtained via the Ghost Fluid Method (GFM). The GFM offers a way to capture fluid interfaces, avoiding large unphysical oscillations and reducing the numerical smearing of discontinuous variables. The idea of the GFM is to introduce two sets of variables, for each

separate phase modeled. The governing equation for each field are solved independently and zero level set separates real and ghost zones. Consequently, the task is implementing the GFM method for populating the field variables in the ghost zones of each fluid during each time step.

For smooth well-behaved problems, the method proposed in [47] is the most appropriate. In this approach, in the ghost fluid regions, discontinuous variables across a fluid interface are given using a one-sided extrapolation, and continuous variables are copied from the real fluid on a node by node basis. In this paper the modified GFM for large density differences across an interface developed by [46] is used. In the modified GFM for air-water interaction, the velocity in the ghost-fluid region for the water and the pressure in the ghost-fluid region for the air are extrapolated from their real fluid regions, respectively, while the pressure in the ghost-fluid region for the water and the velocity in the ghost-fluid region for the air are copied from their real fluid regions, respectively.This same approach has been used successfully by [60] and [52] for simulations of multiphase flows with large density ratio.

2.0.9. Local LS method

In order to improve computational efficiency, both level set advection and the reinitialization are implemented on a narrow band tube in the neighborhood of the interface [44]. This reduces the run-time computation costs, and makes it viable to employ high-order schemes since only a small fraction of the LS function is considered and updated in every time step. When the interface moves out of the narrow band, the calculation is stopped and a new band is built with the interface at the center of the band. The computational cost is reduced because a significant smaller amount of values have to be updated at every time step. In this work, the approximation of [44] is adopted.

Narrow bands of different size are constructed and updated following the moving interface. The size of the bands is fixed and their values γ_i's are multiple of grid sizes. In general, only two bands are required, but if the motion of the interface involves sensitive quantities such as derivatives of curvature is necessary to used a third narrower band.

2.0.10. Mass Conserving Method

The volume of fluid method was introduced by [21] and, since its conception has been widely used in several works. In VOF method, the computational domain is divided into small cells. Each cell is assigned a discontinuous concentration function χ representing the volume fraction of one of the fluids within the cell. From these cell fractions, the position of the interface can be determined using an interface reconstruction procedure within each cell that is intersected by the interface.

Because the function is a conservative variable, the method conserve mass exactly. However, despite the accurately mass - conserving properties of the method, the interface reconstruction and the approximations on geometric properties of the interface are computationally expensive, especially in three dimensional simulations.

The volume of fluid method was introduced by [21] and, since its conception has been widely used in several works. In VOF method, the computational domain is divided into small cells. Each cell is assigned a discontinuous concentration function χ representing the volume fraction of one of the fluids within the cell. From these cell fractions, the position of the interface can be determined using an interface reconstruction procedure within each cell that is intersected by the interface.

Because the function is a conservative variable, the method conserve mass exactly. However, despite the accurately mass - conserving properties of the method, the interface reconstruction and the approximations on geometric properties of the interface are computationally expensive, especially in three dimensional simulations.

The MCLS method developed by [35] is based on the idea of mass conservation improving through the use of a explicit function f that directly relates the VOF function to the LS function. To conserve mass, corrections are applied to the LS function ϕ using the VOF function ψ. This is achieve by application of three steps:

- Calculation of VOF function from LS function
- Advection of VOF function
- Correction of function with the advected VOF function

2.0.11. Discretization of the VOF and LS equations

In order to treat correctly the evolution of the LS function, numerical schemes should have enough accuracy. In the present work, like the LS equation, reinitialization equation, and VOF function is advanced by using a using the fifth order WENO scheme in space [44] and third order TVD-RK in time [49].

WENO schemes are high-order finite difference schemes designed for nonlinear hyperbolic conservation laws with piecewise smooth solutions containing sharp discontinuities as interfaces. On the other hand, third order TVD method is generally recommended, since it has the greatest accuracy and largest time step stability region of the TVD schemes. By cause of its large stability region for a sufficiently small time step, it is guaranteed to be linearly stable for a variety of problems.

2.0.12. Surface tension

Free surface flows are most commonly phenomenon driven by the inertia and gravity forces. However, for some fluid flow problems, interfacial motion induced by surface tension may play a significant role, affecting the dynamics of the interface. Surface tension is the result of attractive forces between fluid molecules acting in the liquid-air interface. In the slow flow problem such as the liquid drop or the bubble motion, the surface tension effect is important. However, in most natural fluid flows the surface tension can be neglected because of its rapid motion character.

In a more general way surface tension may become important if there is an interface between two fluids and the surface tension force on a fluid particle is significant in comparison to the inertial force being applied to the particle. This relationship of forces is evaluated by the Weber number. The Weber number defined by the liquid density ρ, a reference velocity V, a reference length L, and liquid surface tension σ, $We = \frac{\rho V^2 L}{\sigma}$. The influence of surface tension force diminishes as the value of the We number increase. The relative large value of the We number suggests that for the dam-break problems under consideration in the present work the surface tension effects can be neglected in the analysis of flow motion.

2.0.13. Vortex identification

During breaking, the organized and mainly irrotational motion of the waves is transformed into vorticity, turbulence, and irregular patterns. Broken waves involve motions of different types and scales, including large-scale structures, also called "coherent vortical structures" and small-scale turbulence with random motion that appears once these coherent structures have vanished.

Identification of vortices is necessary for understanding the complex flow beneath of breaking waves. The Q-criterion proposed by [61] is one of the most common vortex identification techniques to investigate the generation, evolution and fate of turbulent coherent structures. This criterion is based on a balance between shear strain rate and vorticity magnitude, defining vortices as areas where the vorticity magnitude is greater than the magnitude of rate-of-strain. In this work the Q-criterion is adopted to identify and educe the vortex motions and their evolutions in space and time during a plunging breaking wave.

Chapter 3.

Validation

Validation is a fundamental step in assuring that the numerical code not only works properly, but even more importantly, in assessing the accuracy dependence with varying grid density and with parameters of the numerical scheme and its implementation. For instance, validating turbulence models, two-phase models, empirical data related to real gas effects, temperature dependence of viscosity, etc, can only be achieved by comparing with experimental data.

One of the most popular suitable test cases to prove the capabilities and the performance of a free surface model is the dam break problem. This problem refers to the gravity-driven flow of a fixed volume of fluid suddenly released. For this particular free surface case, a rectangular water column is initially supported by a gate that suddenly is removed. The column subsequently collapses due to gravitational acceleration force and eventually comes to rest and occupies the bottom of the tank. In this work, a three dimensional model is considered in order to reproduce the experiments developed by [62], [63] and test the ability of the numerical code to deal with strong free surface deformation patterns, such as splashing, sloshing, etc. These validation tests cases produced a variety of data so that many aspects of the model can be assessed.

The water column has the properties; $\rho_w = 998.0\frac{kg}{m^3}$ and $\mu_w = 1.13710^3 Pa \cdot s$, while the surrounding air phase has $\rho_a = 1.2\frac{kg}{m^3}$ and $\mu_a = 1.7810^5 Pa \cdot s$. The surface tension coefficient is $\sigma = 0.0728\frac{N}{m}$. The height of the initial water column L is taken as characteristic length and the celerity $V = \sqrt{gL}$ as the reference velocity.

The simulation parameters used for the test cases are summarized in Table 3.1

Test Case	DB1	DB2
Reference Lenght (L) $[m]$	0.3	0.55
y^+	50	75
Total grid number	3,900,000 (52015050)	9,477,000 (58518090)
$Re = \frac{\rho L v}{\mu}$	5.1410^5	1.2710^6
$Fr = \sqrt{\frac{V}{gL}}$	2.0	2.0
$We = \frac{\rho V^2 L}{\sigma}$	1.210^4	4.1110^4
Simulated Time $[s]$	2.0	5.0
CPU Time $[hrs]$	20	85

Table 3.1.: Numerical parameters for validation tests case simulated

In order to characterized the possible impact of the surface tension an order of magnitude analysis of the We number has been carried out. The We number, is large enough to considerer that for the dam-break problems under consideration in the present work the surface tension effects can be neglected in the analysis.

For gravity current flows over a horizontal bed that initiated from rest, such as dam-break the Froude number Fr is technically equal to one regardless of the initial water depth in the dam reservoir. However, in this study the Fr is based on an approximation of the maximum velocity of the fluid wave estimated as $V_{max} = 2.0\sqrt{gL}$ [64], therefore Fr is set equal to 2.0.

3.0.1. Dam breaking (DB1)

The first test based on the classical dam-break flow over a dry horizontal has been taken from the recently experiments performed by [62]. This study provides detailed data in terms of water heights and pressure measurements. The water height has been measured in the positions H1-H4 at different locations along the tank and some pressure sensors are placed in the positions P1-P4, on the solid vertical wall opposite to the initial column of water. The test case configuration and measurement points are shown in Fig. (3.1).

Although measurements of the exact interface shape are no available, Fig. (3.2) shows a sequence of snapshots of numerical and experimental free surface profile evolution at different times.

The temporal evolution of the free surface deformation keeps good agreement with the experiment images and some important flow features are accurately identified: Initial

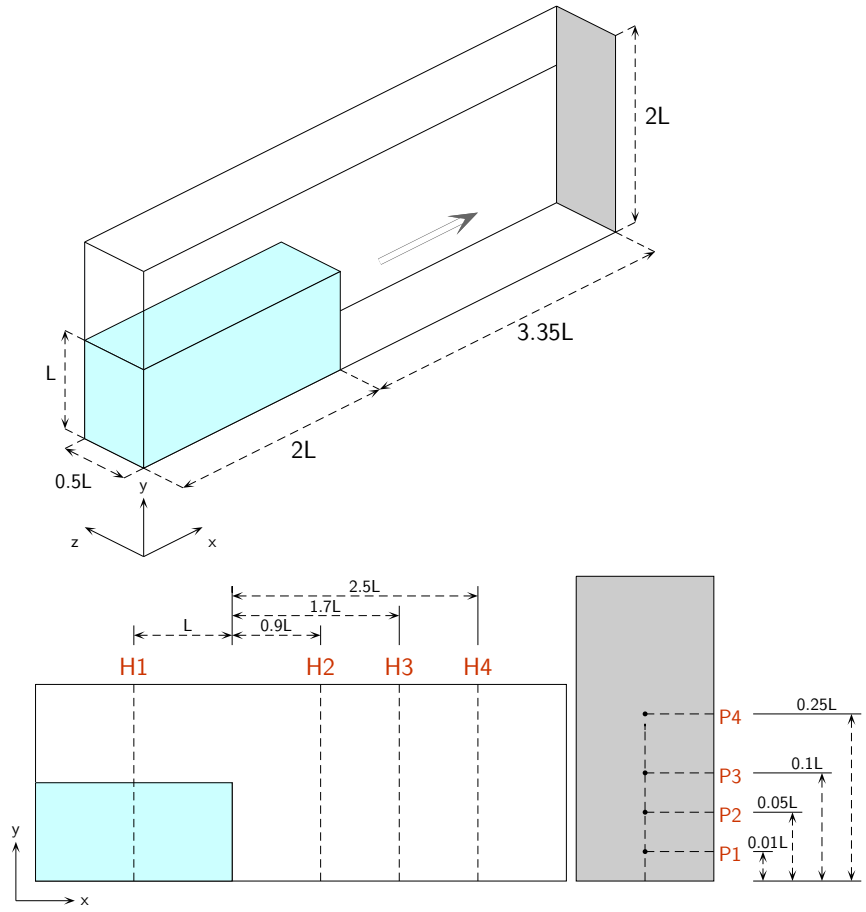

Figure 3.1.: Schematic view of dam-breaking flow testing case.

water column (a), as the time progress, the collapsed water moves to the right (b-d), and at the time (e-h) the flow impacts the vertical right side wall forming an upward water jet that falls down due to gravity effects and forms a plunging wave. Finally a high turbulent wave continues moving to the left (i-k). However, because of the insufficient grid resolution, some fine details such droplets and bubbles are not well captured by the simulation.

Figure 3.3 compare the time evolution of water level at locations H1-H4. A general good agreement is found between measurements and simulations, especially at early times, after that, differences between the two solutions occur. The plunging jet resulting from the impact against the right wall, splash-up and induce the formation of vortical structures creating a complex flow with a large free surface deformation. The major discrepancies are presented at locations H3 and H4, that is, the nearest locations to the splash-up region. At this locations, the water level is underestimated. This situation can be understood because the maximum experimental height considers the fragmented fluid

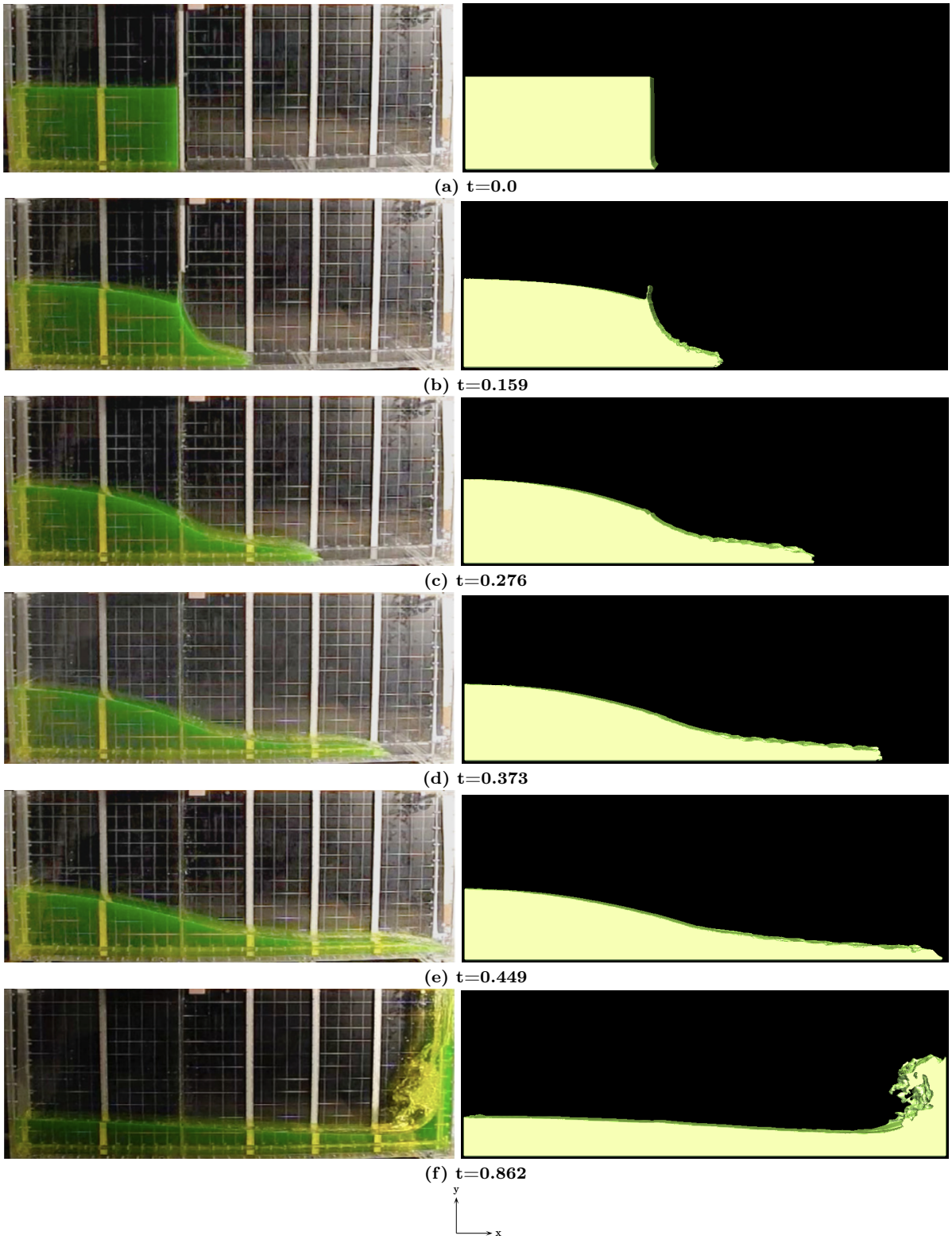

(a) t=0.0

(b) t=0.159

(c) t=0.276

(d) t=0.373

(e) t=0.449

(f) t=0.862

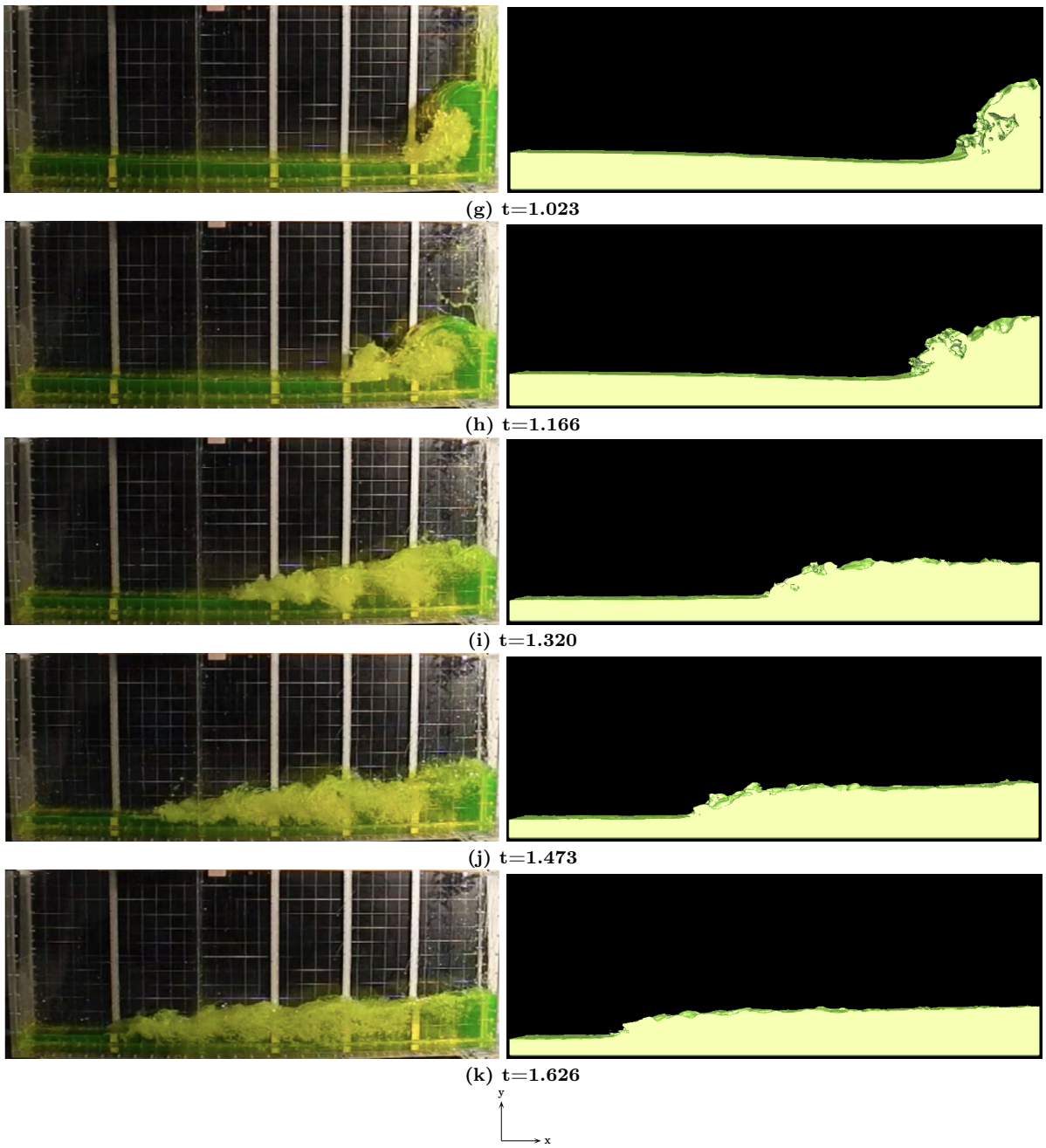

Figure 3.2.: Snapshots of numerical and experimental dam-break flow. Experimental snapshots taken from [62]. Time in seconds.

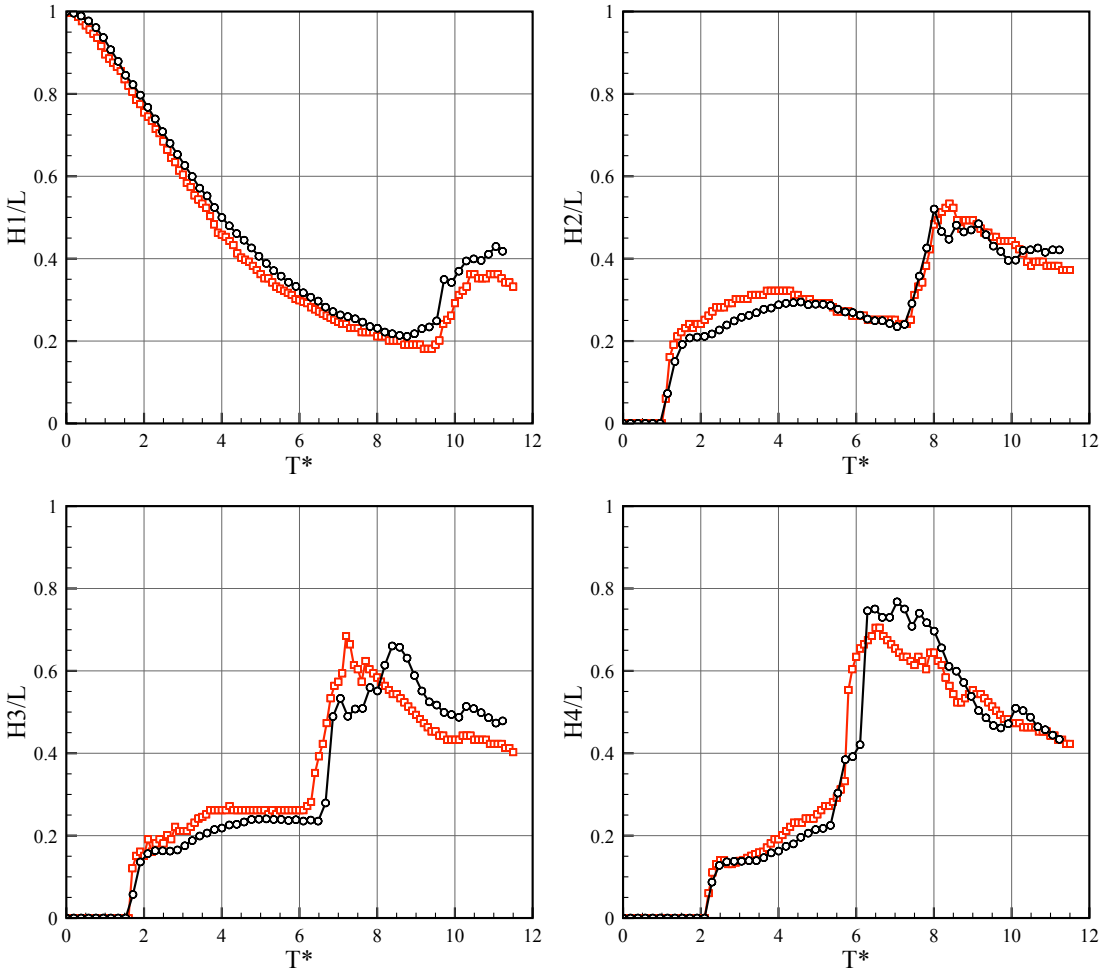

Figure 3.3.: Predicted and measured free surface elevations time histories at H1-H4. Black circle (experimental); Red square (numerical).

particles detached during the jet impact and that are not captured in the simulation. The discrepancies in the elevation of the secondary wave arise from the complex flow structures that are created as the secondary wave propagates through the tank.

Figure 3.4 compares the time histories of pressure at locations P1-P8. The pressure, P, is non-dimensionalized considering the hydrostatic pressure at the bottom of the reservoir as the reference pressure. The agreement between the simulation and the experiments is very good capturing correctly the first and second pressure peaks that are observed in the experiment. However, numerical results presents some fluctuations and the predicted maximum is overestimated, especially at sensor P1 and P2, while major discrepancies are presented at location P4, that is, the sensor located at the highest position. At this sensor location, the predicted maximum is underestimated. This is linked to the fact that the flow in the jet formation is more complex.

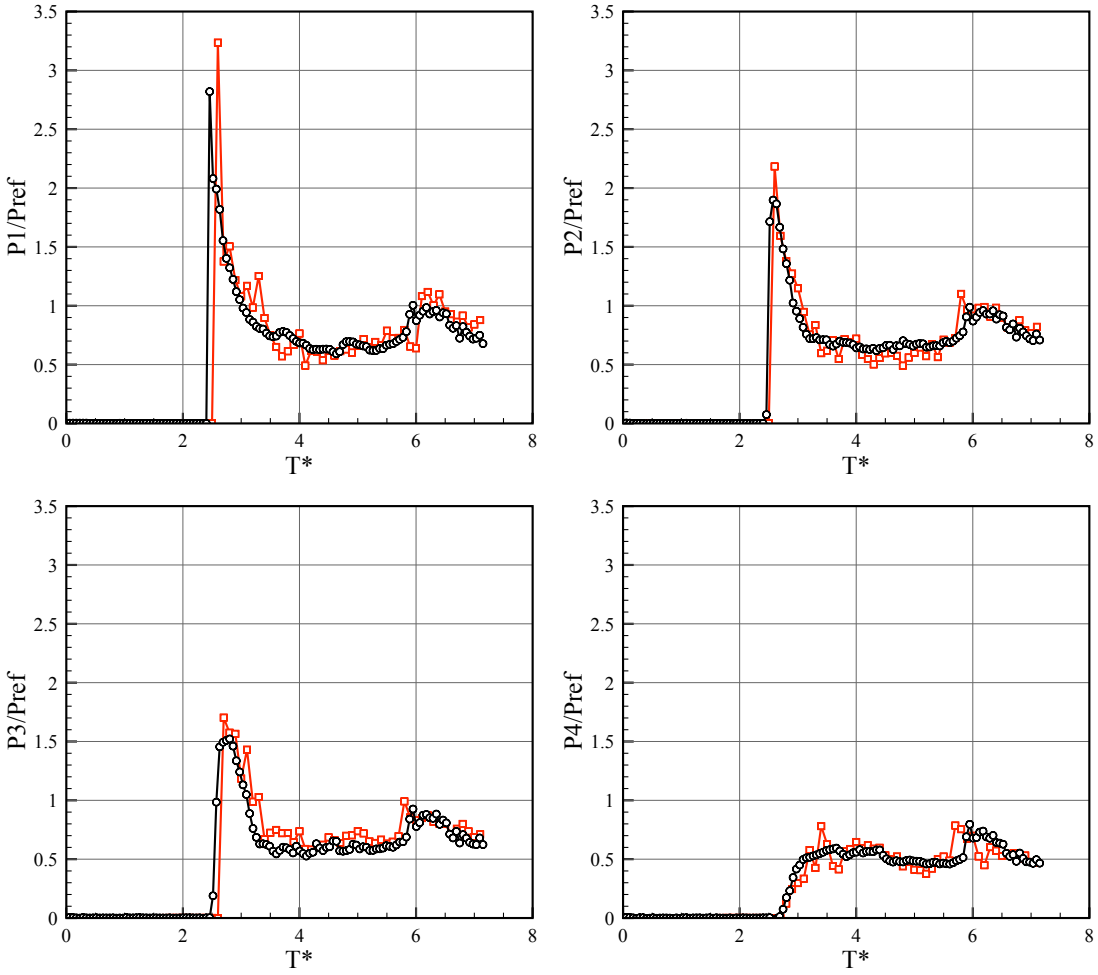

Figure 3.4.: Predicted and measured pressure time histories at P1-P4. Black circle (experimental); Red square (numerical).

3.0.2. Dam breaking over an obstacle (DB2)

The second benchmark test developed by [63] is performed to demonstrate the ability of the numerical model to capture 3D deformations after the violent interaction between the free surface and a rigid body. The experiment consisting in the collapse of a column of the water that impacts a stationary obstacle at the bottom of the tank is a benchmark test case, since plenty experimental data are available in terms of water heights and pressures at different locations of the tank and obstacle. Fig.(3.5) shows a schematic view of the domain setup and the locations of the height sensors H1-H4 and the pressure sensors P1-P8 for the present simulation. The dimensions, geometry and initial conditions of the problem correspond to those used in the experiment. No-slip boundary conditions have been applied to the bottom and sides of the tank; slip boundary conditions have

been applied to the front and back face of the tank. The obstacle have been numerically modeled by the immersed boundary method according to [59]. Because of lack of information of gate opening speed, water is released immediately when the simulation is started.

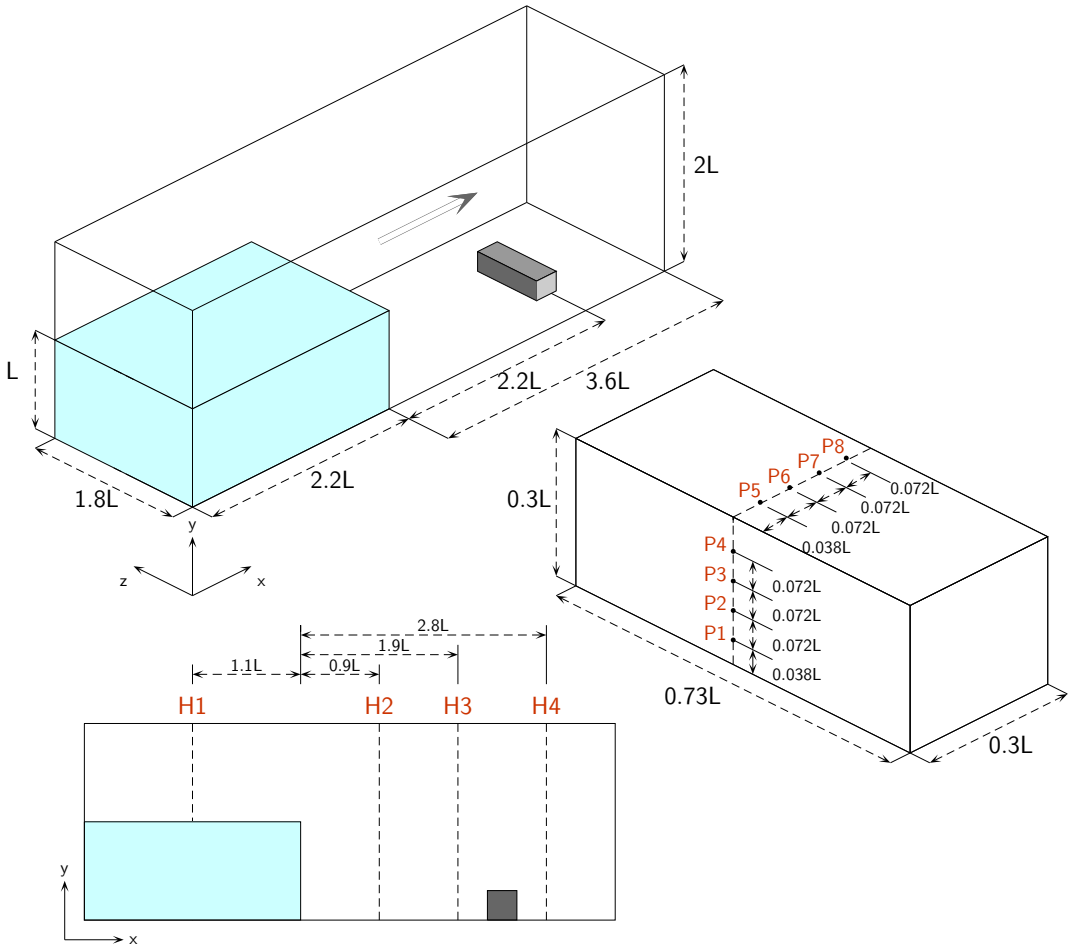

Figure 3.5.: Schematic view of dam-breaking flow testing case.

Fig. (3.6) shows a sequence of snapshots of water evolution in the present simulation together with experimental images at different times. In general, a good agreement between the numerical simulation and experiment was obtained. Numerical predictions shows an unsteady behavior of the free-surface flow with interface ruptures and coalescence after the impact with the obstacle. The flows become chaotic and complicated due to the effect of the obstacle and the tridimensionality of the phenomenon. Because the grid mesh size the numerical model is not able to capture the drops that emerge after impact.

The time histories of free surfaces elevations at the locations $H1 - H4$ are depicted in Fig. (3.7). A general good agreement is found between measurements and simulations.

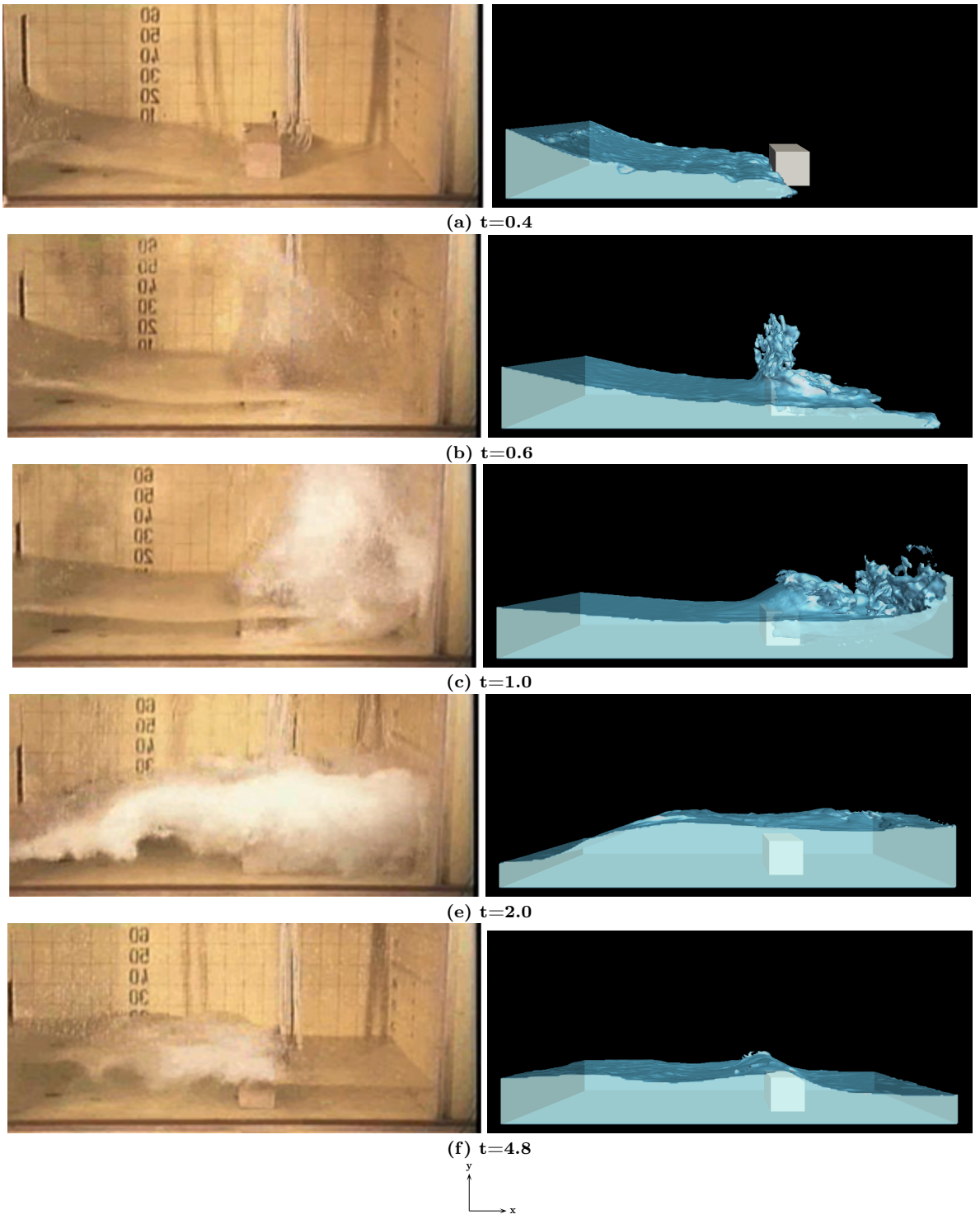

Figure 3.6.: Snapshots of numerical and experimental dam-break flow. Experimental snapshots taken from [63]. Time in seconds.

At probe point H1 at early times the water surfaces elevation is almost exactly the same in simulation and experiment, though there is some differences in the maximum water height. At probe points H2 and H3, numerical result is delayed about one non-dimensional time, while predicted water surface elevation by numerical model appears to be higher than that by the experiment. On the other hand, at probe point H4 predicted water surface elevation by numerical model appears to be lower than the experiment. The reason is that, at the vicinity of the obstacle the flow structure is more complex, and the predicted free surface elevation by numerical model presents strong fluctuations especially after water impact the obstacle.

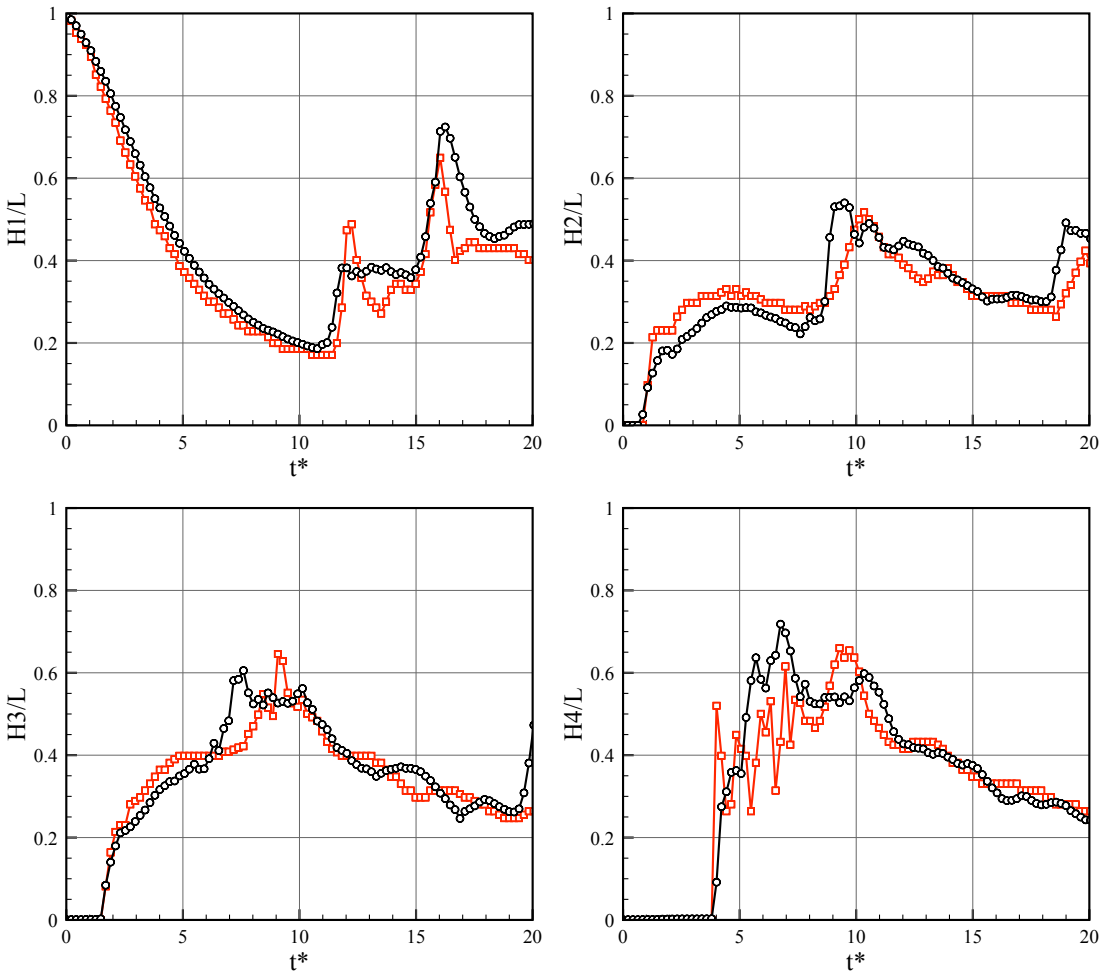

Figure 3.7.: Predicted and measured free surface elevations time histories at H1-H4. Black circle (experimental); Red square (numerical)

For the purpose of analyzing the ability of the numerical model to predict the loads exerted by the fluid on solid surfaces, pressure at different positions of the block is obtained. The time histories of pressure at locations P1-P8 are depicted in Fig. (3.8).

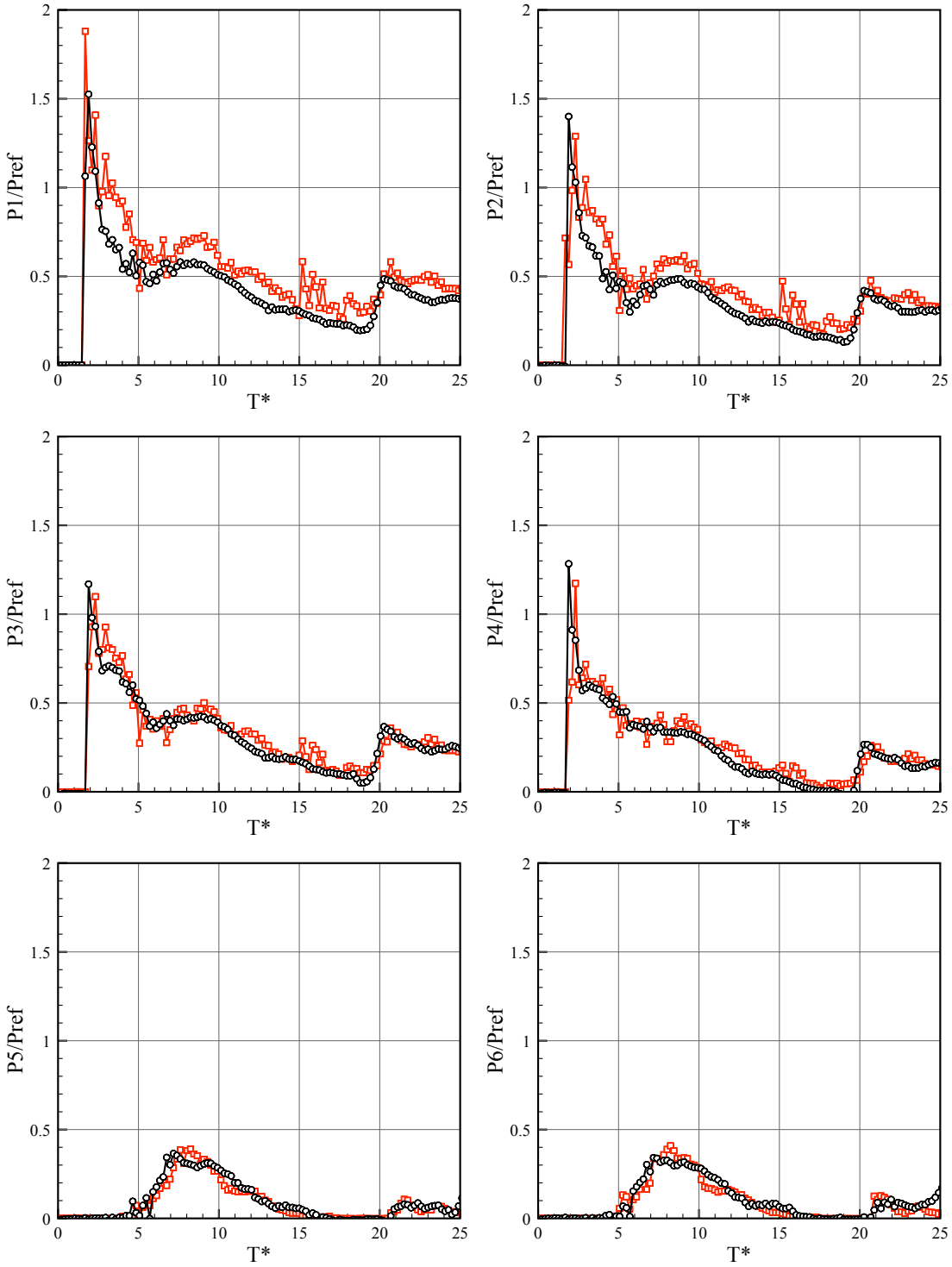

Figure 3.8.: Predicted and measured pressure time histories at P1-P8. Black circle (experimental); Red square (numerical).

Pressure predictions provide a general good agreement with the experimental data. The maximum numerical and experimental values of pressure, which correspond to

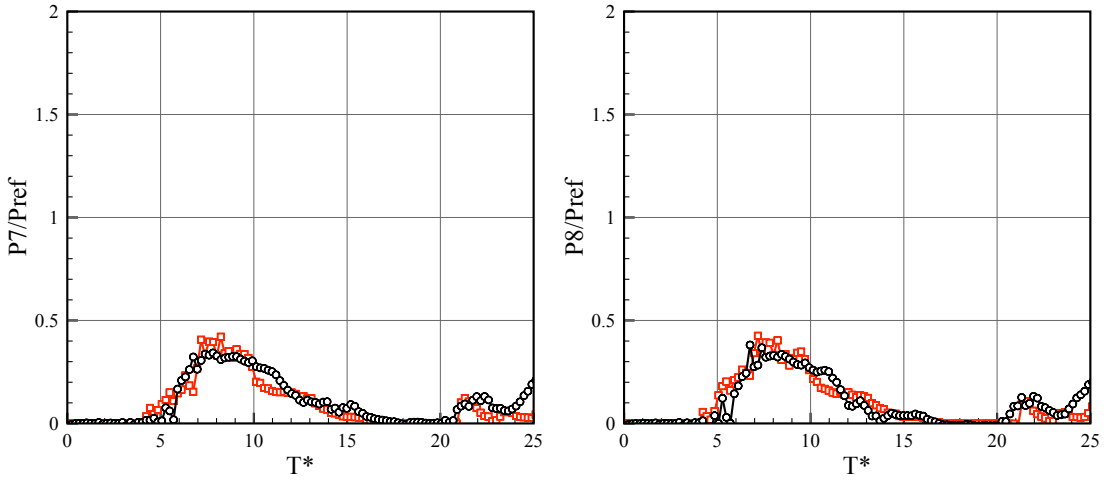

Figure 3.9.: Predicted and measured pressure time histories at P1-P8. (continued)

first water impact on the obstacle, coincide in magnitude and time with respect to the experimental one. The only important difference is observed at probe point P1 where pressure predictions from the numerical model is slightly higher than the experimental results. For P1 and P2, pressure predictions from numerical model shows over-predicted pressure with strong fluctuations after water impact the obstacle. Although the tendency is almost the same.

The agreement between the numerical and experiment results is satisfactory, which shows that the numerical approach is capable of accurately and robustly handling with large-deformation free surface flows with and the violent interactions between free surface and stationary rigid body in three dimensions. Besides, the numerical model is suitable for the applications in ocean engineering problems, e.g. breaking waves dynamics.

Chapter 4.

Breaking wave simulation

The study of dam-break flow has been a topic of significant research for both practical and academic interests due to its relevance to environmental and structural damages caused by the wave impacts. In the context of numerical studies of dam-break flows have become an attractive and cost-effective way to evaluate the performance of the interfacial simulation codes. These studies have been focused on the accurately description of the free surface evolution and water front displacement over a dry bed, where the wave front moves quickly with not appreciable turbulence and free of any breaking process. However, If there is initially a fluid layer in the channel, the behavior of the flow becomes much more complex, even in the presence of a thin layer. The static layer at the bottom resists to a quick replacement of the wave front producing a propagating bore that evolves until a single plunging wave breaker event occurs.

[18], [19] and [20] have conducted dam-break experiments with a wet-bed condition downstream of the initial water column. [18] focus on turbulence characteristics on the early stage of the dam break flow; [19] studied turbulence drag reduction due to the addition of polymer in their experiments. [20] used a dam-break mechanism for studying the bore collapse and the evolution of bed shear stress during the swash motion over an impermeable slope. The dam-break study presented by [20] have shown that dam-break experiments can be successfully used for modeling fluid dynamics of a single plunging breaking wave and for the study of coastal hydrodynamics processes in general.

Considering the distinctive features of a dam-break flow reported in the a-foregoing studies, in this work, the generation and evolution of turbulent coherent structures under a single plunging breaking wave generated by a dam-break event with a wet-bed condition downstream is numerically investigated. The main advantages behind studying a single breaking event is that the breaking wave process and the generation and evolution of

the associated turbulent structures can be investigated separately from the effect of returning undertow flow and the residual turbulence induced from previously broken waves in the case of periodic waves and a single breaking wave results less computationally time comparing to periodic wave conditions and hence it allows for the use of a higher numerical resolution on critical regions.

4.1. Dam breaking with a wet-bed downstream condition

The validity of the present numerical model has been examined previously [65]. However, this work attempts to represent in the most approximate way the whole experimental wave-breaking process, therefore, a further validation is performed and unlike previous works, some important initial features, such as, gate motion and gravity effects are considered in the analysis.

The numerical study is based on the experiments of [19]. Figure 4.1 shows a schematic view of the domain setup for the present simulation where the dimensions, geometry and initial conditions of the problem correspond to those used in the experiment. The simulation was conducted for one initial depth ratio condition only: $\frac{d}{d_0} = 0.1$, with a water depth in the reservoir ($d_0 = 0.15m$). Gate movement is implemented within the immersed boundary method.

4.1.1. Gate effect

For a dam-break problem the movement of the gate represents an important initial condition influencing the collapses dynamics, however, considering the complexity of the experiment, in most of the numerical simulation a sudden gate opening is assumed, i.e, the water column collapse immediately as soon as the computations begins. In this work, the effect of a moving gate is numerically included and considerable attention is paid to the difference in water front toe evolution, free surface profile and breaking onset between dam-break simulation for gate/no-gate cases.

According with experimental data from [19] the gate moves vertically with an uniform velocity of $1.5\frac{m}{s}$. Taking the initial water depth in the reservoir (d_0) as the characteristic length and $\sqrt{gd_0}$ as the characteristic velocity, $Fr = 1$ and $Re = 185800$.

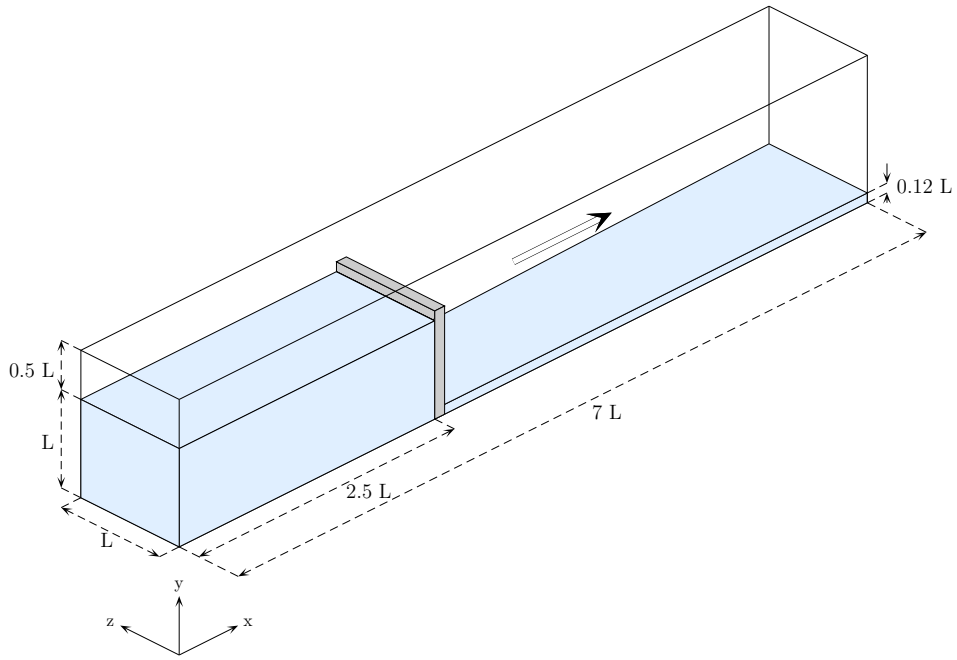

Figure 4.1.: Schematic view of dam-breaking flow over a wet-bed testing case.

Figure 4.2 shows experimental snapshots and numerical predictions for no-gate case at different instants of the dam-break evolution.

Figure 4.3 shows experimental snapshots and numerical predictions for gate case at different instants of the dam-break evolution.

Analyzing the different instants: after the water column initially placed behind the gate pushes the shallow water layer, a propagating bore develops; the resistance of the shallow water layer generate a unstable configuration, reported by [18] and [19] as "mushroom-like" water jet where a wave breaking in both (forward and reverse) directions occur; the more prominent forward breaking breaks about $0.06s$ after the backward breaking in form of a plunging jet with enough energy to generate a second breaking event with a similar size.

Simulations show the main features observed in the experimental snapshots. The numerical model reproduces from the wave propagation to the formation of the mushroom-like water jet and the subsequent wave breaking phenomena with reasonable accuracy. However, the overall agreement is not satisfactory. Looking at the shape of the water surface front, the experimental and gate numerical results show a similar shape, while the difference in the front free surface shape is found to be more distinct when gate movement is not considered, especially at the initial stages. For the latter stages all surface shape

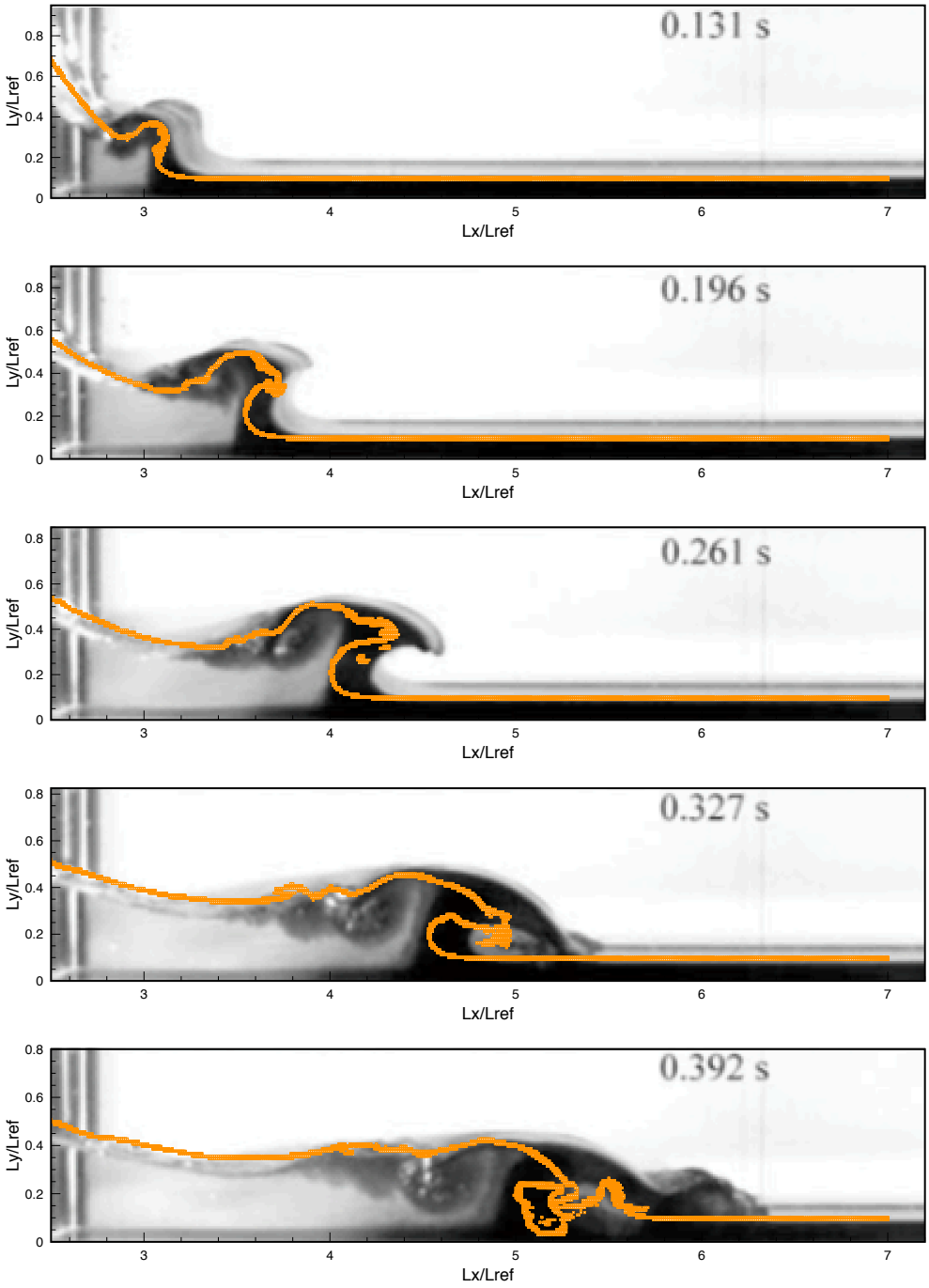

Figure 4.2.: Experimental snapshots and numerical predictions for no-gate case at different instants of the dam-break evolution

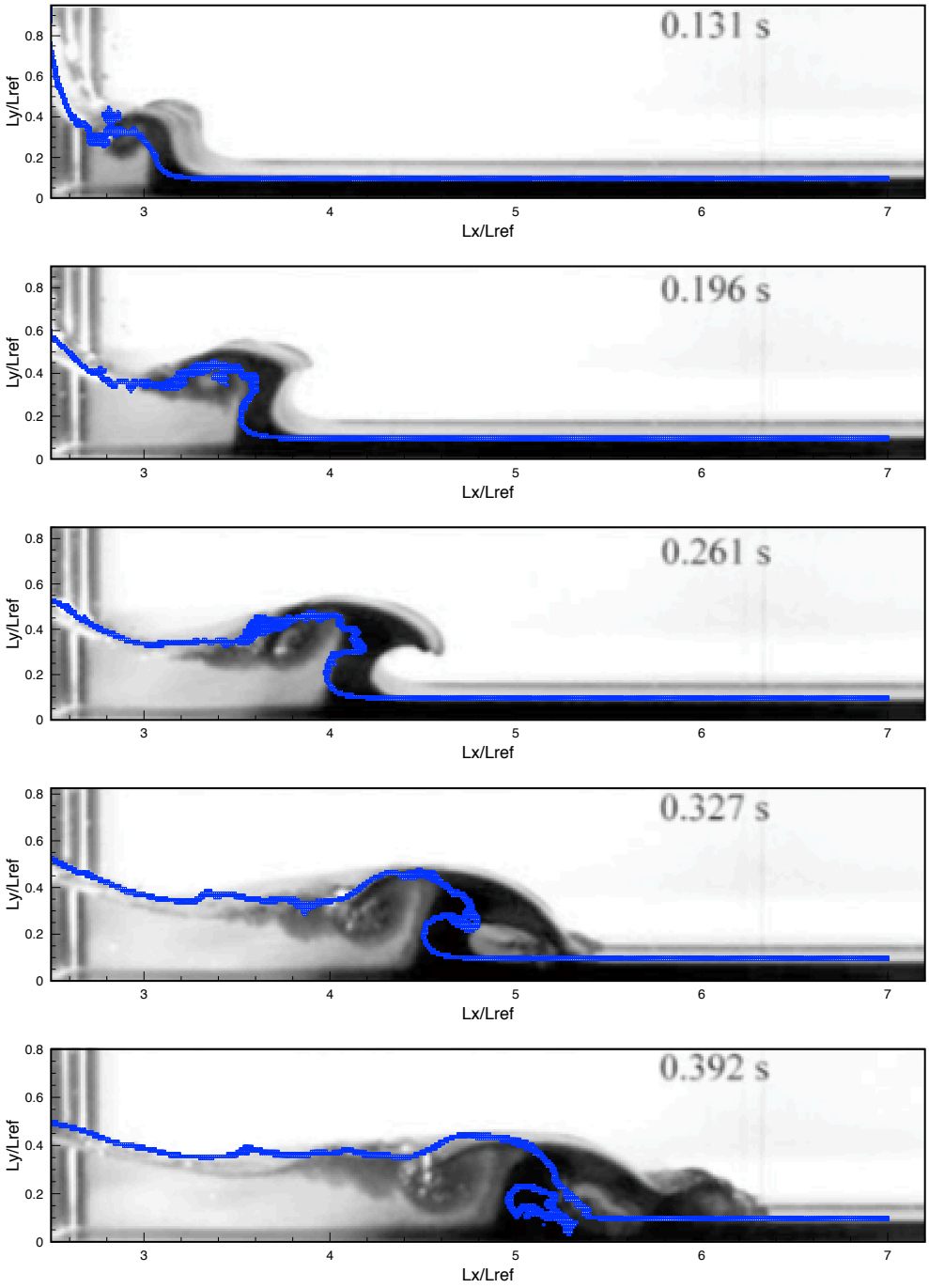

Figure 4.3.: Experimental snapshots and numerical predictions for gate cases at different instants of the dam-break evolution

representations become close, however the displacement of the experimental wave front runs always ahead of the numerical predictions, in addition gate simulation shows an evident time delay with respect to the experimental results. According to experimental data the first plunging jet impact presents at $t = 0.327s$, however the gate simulation the impact happens about $0.07s$ latter.

4.1.2. Gravity effect

In general, simulations shows similar patterns observed in the experiment. However, both gate and no-gate show evident differences with respect to the experimental results. Despite the fact that the differences could be explained as the result of experimental factors than cant be exactly reproduced on the numerical model such as the gate removal technique or physical properties of gate and tank floor. It is important to point out that in the above simulations the Froude number (Fr) a characteristic parameter in gravity driven flows, is equal to one regardless of the initial water depth in the dam reservoir. However, unlike the dam-break flow over a dry bed where the forward momentum generated for the initial water column dominates the fluid movement, dam-break over a wet bed is characterized by a strong interaction between upstream (d_0) and downstream (d) columns, therefore, the physical characteristics of the propagating bore over a layer of constant depth d, with a speed U_m must be considered.

For a dam-break problem over a wet bed the theoretical Fr, the water depth below the wave front d_m and the propagation celerity U_m are related by the theoretical hydraulic jump formula.

$$Fr = \frac{U}{gd_0} = \frac{1}{2}\frac{d_m}{h_0}\left(\frac{d_m}{d_0} + 1\right) \tag{4.1}$$

where d_m is determined from the initial condition using the dam-break solution as given by [66]

$$\sqrt{d} = \sqrt{d_m} + (d_m - d_0)\sqrt{\frac{d_m + d_0}{8d_m d_0}} \tag{4.2}$$

The Fr corrected value based in the above analysis for the dam-break depth ratio condition: $r = \frac{d}{d_0} = 0.1$ considered in this study is $Fr = 3.1$. Figure 4.4 shows experimental snapshots and numerical predictions at different instants of the dam-break evolution considering gate movement and Fr correction.

Results considering the Fr correction show a satisfactory agreement with the experimental results. Numerical height and location of the wave front match closely with the the experimental snapshots. Mayor discrepancies lie in the amount of water at the surface of the rebound jet after the first plunging jet impact. The experimental snapshot suggests that the the rebound jet makes up approximately half of the first wave column, whereas the numerical prediction underestimates the amount of mixing upstream of the wave front. On the other hand, back wave bore elevation appears to be lower than the one obtained by the experiment.

The numerical model has been shown to reproduce the experimental profiles accurately, however is important to considerer that with the increasing depth ratio condition the interaction between the two water layers exhibit different patterns. Depth ratio condition determines the shape of the propagating wave front, the wave front behaves and the subsequent wave breaking characteristics, therefore, in order to verify Fr correction validity, several different downstream depths, from a shallow to deep downstream conditions are considered. Based on Eq. 4.1, a particular Fr value for each depth ratio conditions r is determined.

Figure 4.5 presents the experimental snapshots and numerical predictions at an initial time $t = 0.3s$ for different downstream conditions cases.

Depending on the depth condition, different propagation regimes have been observed. Because the large pressure gradients the water wave front breaks almost immediately under a shallow downstream condition. While for a depth downstream condition the displacement of the water wave and the fully develop of the bore is slower and the wave fronts are still gaining their height at this instant. Only wave breaking is observed for the $r = 0.03$ depth ratio condition. Consistent with previous results, good agreement is found between the experimental snapshots and numerical predictions with just a few discrepancies for the nearly dry-bed conditions.

The study shows that the predicted gate motion matches well with the experimental results and emphasizes the influence of the gravity effects on wave propagation.

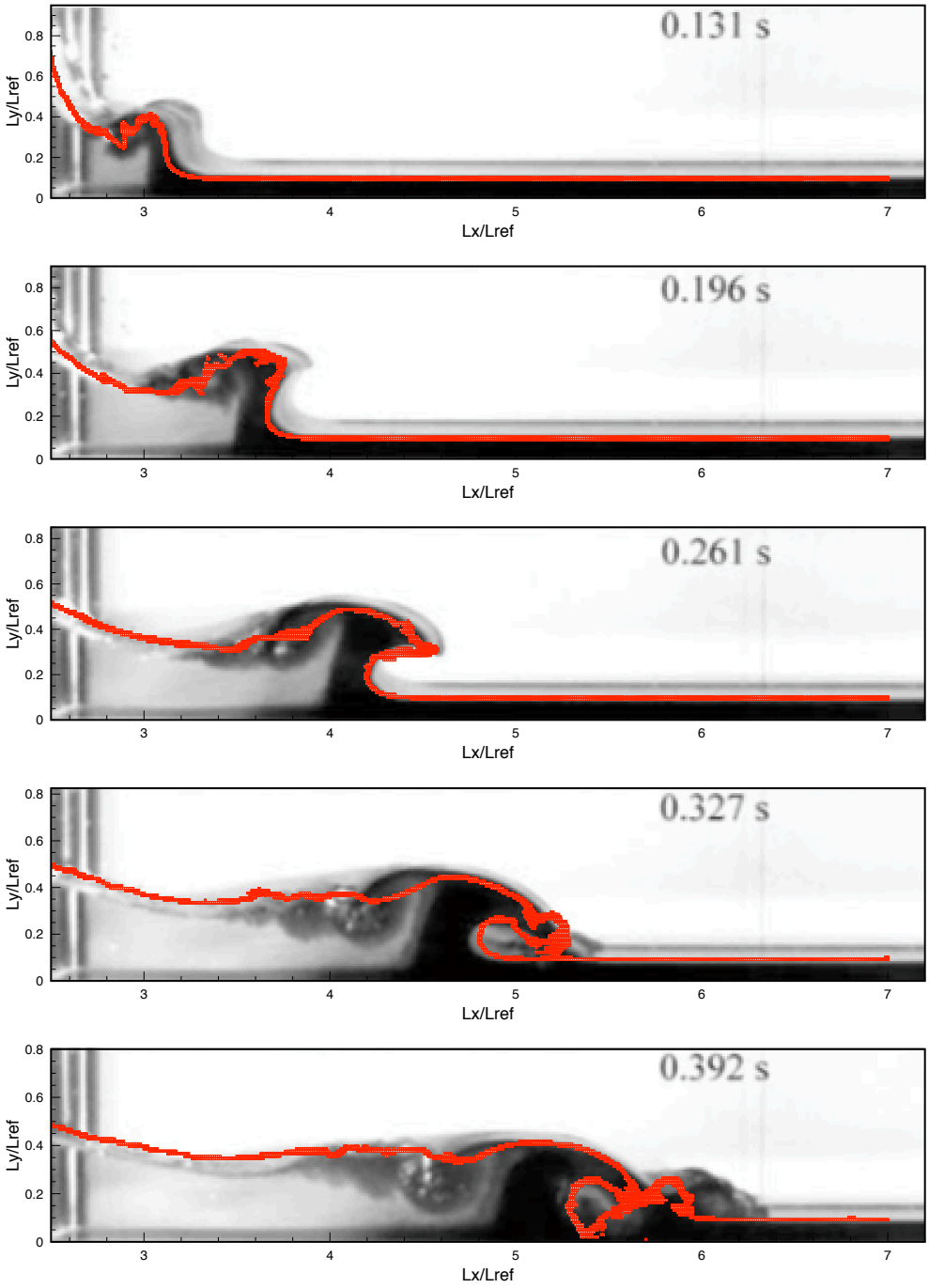

Figure 4.4.: Experimental snapshots and numerical predictions at different instants of the dam-break evolution with Fr correction.

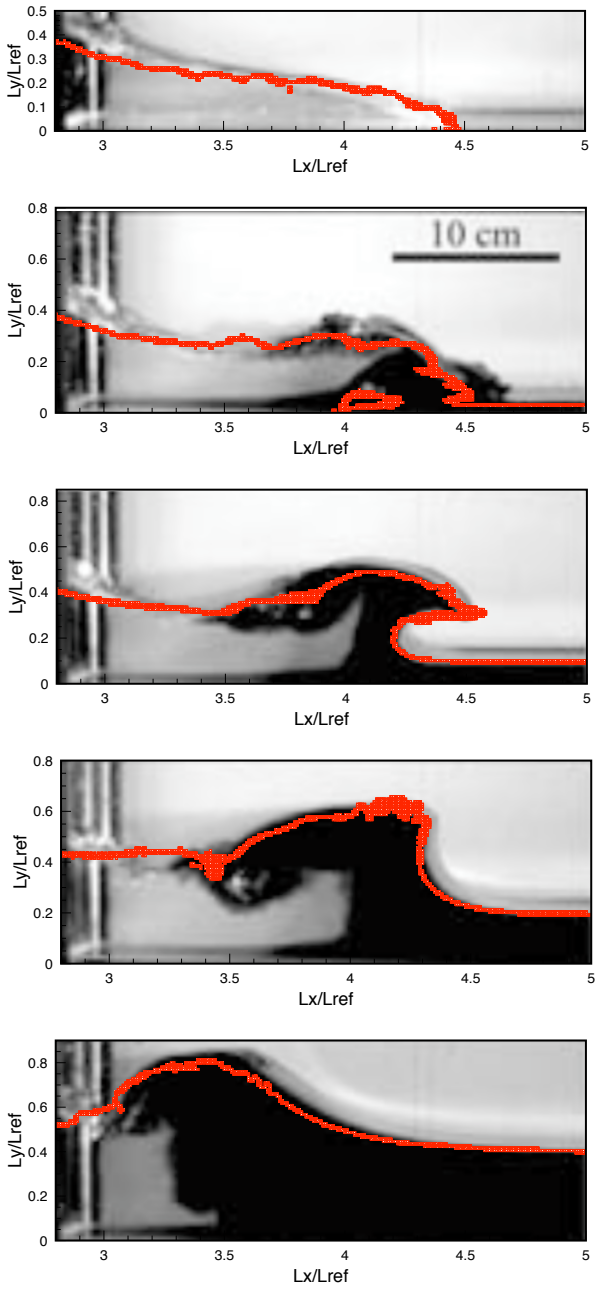

Figure 4.5.: Experimental snapshots and numerical predictions for different depth conditions cases ($t = 0.3s$)

4.2. Breaking wave turbulence

During a breaking wave the organized and mainly irrotational motion of the incoming wave is transformed into a significant amount of turbulence characterized by irregular patterns motions of different types and scales, including large-scale structures, also called "coherent turbulent structures" and small-scale turbulence with random motion that appears once these coherent structures have vanished.

Now that the numerical model has been shown to provide accurate results on dam break propagation over a wet bed under different depth conditions r, it can be used for simulating and analyzing the dynamics of the propagation wave and the process of a single plunger breaking event. Special attention is paid on the identification of the coherent vortical structures generated during and after the plunging jet impact.

Based in the previous sections analysis the best conditions for analyzing a single plunging breaking wave event have been determined and some considerations have been made in order to increase computational efficiency:

- Only a shallow depth condition is tested, since the development of the jet breaking process is faster under these conditions. The breaking process is delayed when increasing r.
- A shorter computational domain is adopted, since only the first forward impinging jet is of interest for significant vortical flow motions and turbulence generation.
- The upstream water column base length is reduced to $0.15m$, since base length has a minor effect in wave propagation and the breaking process.

The simulations are performed for a single depth ratio condition $r = 0.15$. No slip boundary conditions have been applied to the bottom, front and back face of the tank; slip boundary conditions have been applied to the sides of the tank. The gate of the tank has been included in the simulation so that the experimente could be reproduced accurately. Gate is removed from above at constant velocity $V = 1.5m/s$ which would take a time $0.1s$. The water columns have the properties; $\rho_w = 998.0\frac{kg}{m^3}$ and $\mu_w = 1.13710^3 Pa \cdot s$, while the surrounding air phase has $\rho_a = 1.2\frac{kg}{m^3}$ and $\mu_a = 1.7810^5 Pa \cdot s$. The surface tension coefficient is $\sigma = 0.0728\frac{N}{m}$. The height of the initial water column L is taken as characteristic length and the celerity $V = \sqrt{gL}$ as the reference velocity. The simulation parameters are summarized in Table 4.1

Test Case	DB1
Reference Lenght (L) $[m]$	0.15
Total grid number	16,800,000
	(800140150)
$Re = \frac{\rho L v}{\mu}$	1.8110^5
$Fr = \sqrt{\frac{V}{gL}}$	2.74
$We = \frac{\rho V^2 L}{\sigma}$	3.010^3
Simulated Time $[s]$	0.6
CPU Time $[hrs]$	100

Table 4.1.: Numerical parameters for breaking wave simulation

Fig.(4.6) shows a representation of the various physical phenomena and flow patterns distinctive of a breaking wave flow: the formation of a forward vertical crest front traveling downstream; a first weak backward breaking due to the resisting effect of the still water; the development of a forward breaking in the form of a overturning plunging jet and a splash of water after jet impact.

The numerical model consistently reproduce the major features of the expected free surface evolution observed in the experiment of [19]. However the attention is focus on the complex vortical flow generated during the forward plunging wave breaking. The Q-criterion proposed by [61] is one of the most common vortex identification techniques to investigate the generation, evolution and fate of turbulent coherent structures. Based on the Q-criterion some characteristic features and well-defined vortex structures have beed identified.

Fig.(4.7) shows sequences of the computational free surface and the vortex structures visualized by $Q = 100$. Two coherent turbulent structures have been identified. The first turbulent coherent structure is what commonly known as a hairpin vortex or horseshoe vortex usually presented under broken solitary wave [67]. This structure appears in the impact zone and could be the result of the arrangement of scars or finger on the upper surface of the jet. On the other hand, the plunging jet forms an inner non-circular shape air tube where the trapped air is quickly compressed by water beneath the crest. The water circulation around the tube induces the formation under the impact zone of some aerated vortex filaments similar to the rib-like vortex structures identified by [15]. This turbulent coherent structure with a short existence is connecting the main tube air with the rebound splash-up and the secondary jet.

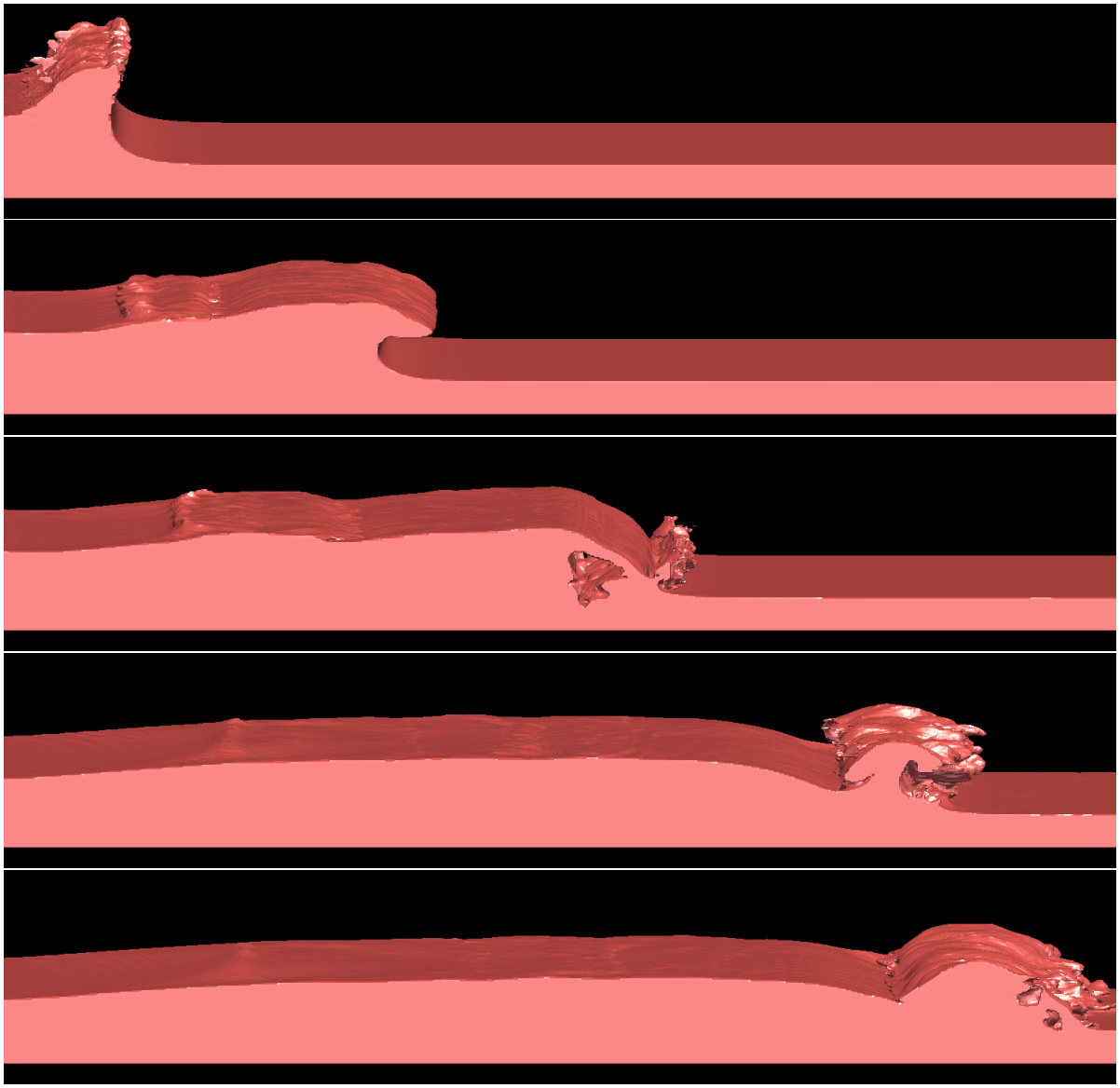

Figure 4.6.: Breaking wave sequences. Air-water interface is identified by the zero level set function

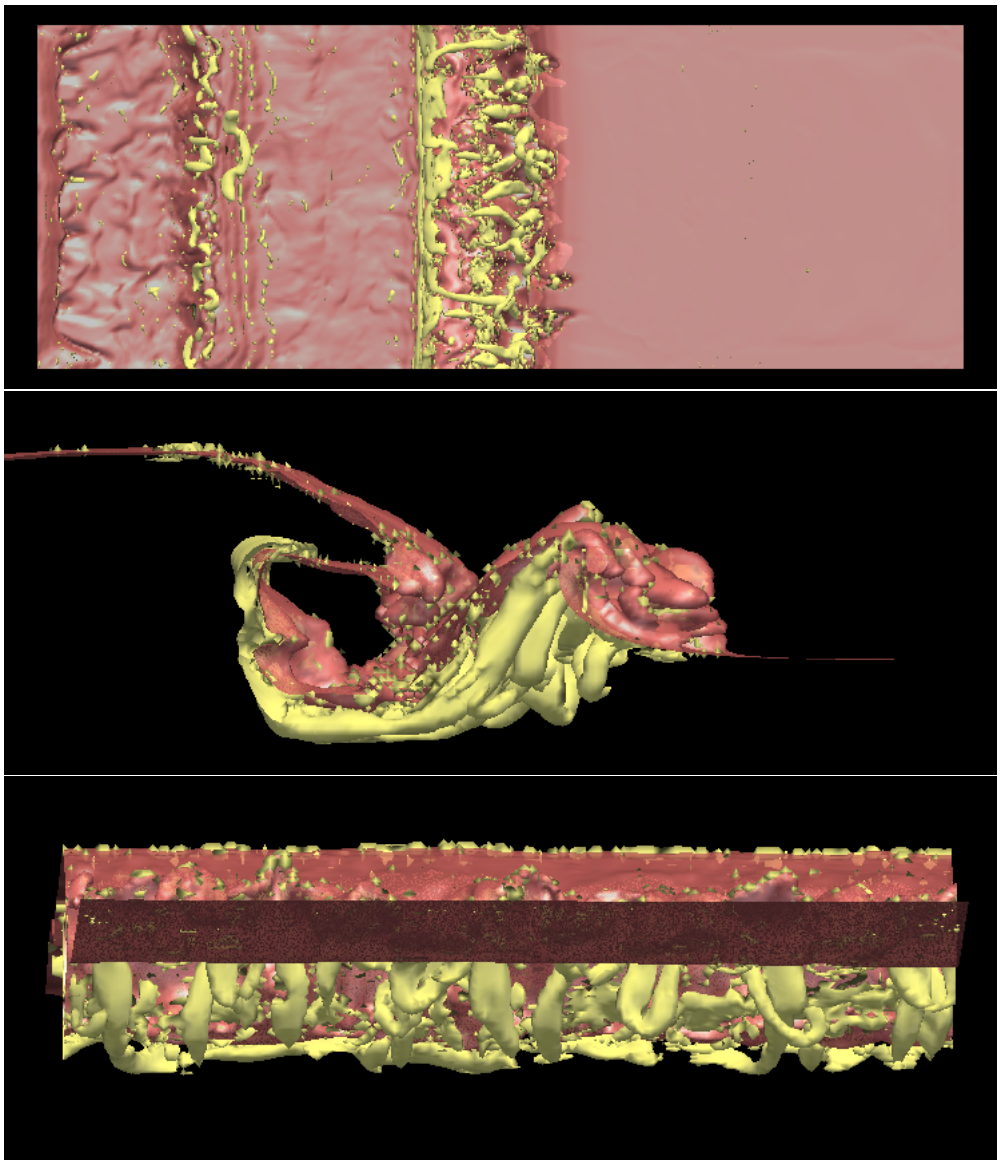

Figure 4.7.: Vortex structures visualized by $Q = 100$ during plunging impact

After the first rebound splash-up, a bore with a significant amount of turbulence is generated. This constitutes a main mechanism of vorticity production, however no distinctive turbulent structures have been identified.

Chapter 5.

Conclutions

An efficient two-phase LES method for simulation of incompressible free surface flows has been presented. The method combines the strengths of both the LS and VOF methods, for capturing a sharp interface accurately and improving mass conservation. The numerical model proposed has been validated against three benchmark test problems: classic dam break flow, dam break flow over an obstacle, and dam break flow over a wet bed. The three benchmark test problems have been fully three-dimensional simulated.

Numerical method appears to be well-suited in dealing with two-phase flows with large density ratio and large deformations of free surfaces with accuracy and efficiency. Numerical results predict properly free surface evolution observed in the experiments. Comparisons with experimental data show a good agreement. A contribution of this work is the incorporation of air effect into the solution of the Navier-Stokes equations.

The study of the gate motion effect shows that the predicted gate motion matches well with the experimental results. The water level height and the displacement of the water wave are strongly affected by the gate motion. On the other hand, since free surface flow are strongly influenced by gravity effects, the Froude number is also an important parameter to consider in the simulation.

Numerical results provide an accurate description for both the free surface and the turbulent flow structures. Results are very useful for further development of parametric models for study of highly turbulent flows as breaking waves phenomena in coastal engineering problems. Results represent a database for future analysis of air entrainment during breaking event.

Appendix A.

Numerical model

A three-dimensional turbulent multiphase flow with strong deformations such as wave breaking (e.g. plunging) can be described by the Navier-Stokes equations coupled with a free surface model for capturing interface evolution. In this study, the governing equations are based in a quasi-incompressible formulation, where the solution of both air and water flows are considered in the model. LES methodology is adopted, since this approach provide a sufficient amount of high-resolution information for an adequate description of the generation and evolution of coherent structures. The free surface model is based on a couple Level set- Volume of fluid concept. Surface tension at the interface is neglected.

The full details of the numerical model may be founded in Appendix A. Here, only a partial description of the model is presented.

A.0.1. Compressible Navier-Stokes equations

In a Cartesian frame of reference, the two-phase Navier-Stokes equations can be written in the so-called fast conservation form of [50]:

$$\frac{\partial U}{\partial t} + \frac{\partial F_i}{\partial x_i} = \mathbf{S_F} \tag{A.1}$$

where U is the four component vector defined by:

$$U = (\rho_\lambda, \rho_\lambda u_1, \rho_\lambda u_2, \rho_\lambda u_3) \tag{A.2}$$

Here $u = (u_1, u_2, u_3)$ is the velocity vector and ρ is the density. Equation (A.1) represents the evolution of density (continuity equation) and momentum equation.

F_i are the fluxes where $\forall_i \in \{1, 2, 3\}$, and for a Newtonian fluid are given by

$$F_i = \begin{pmatrix} \rho_\lambda u_i \\ \rho_\lambda u_i u_1 + p\delta_{i1} - 2\mu_\lambda S_{i1} \\ \rho_\lambda u_i u_2 + p\delta_{i2} - 2\mu_\lambda S_{i2} \\ \rho_\lambda u_i u_3 + p\delta_{i3} - 2\mu_\lambda S_{i3} \end{pmatrix} \tag{A.3}$$

Finally, the term $\mathbf{S_F}$ corresponds to the source terms, than represent gravity effect. The subscripts λ in Equation (A.3) denote two different material properties, the liquid and the gas phase, respectively, δ_{ij} is the Kronecker delta and S_{ij} is the deviatonic part of deformation tensor, written as:

$$S_{ij} = \frac{1}{2}\left(\frac{\partial u_i}{\partial x_j} + \frac{\partial u_j}{\partial x_i} - \frac{2}{3}(\nabla \cdot u)\delta_{ij}\right) \tag{A.4}$$

A.0.2. Quasi incompressibility approximation

Incompressible flow is approximated by replacing the pressure in the compressible Navier-Stokes equation according with the equation of state for an artificial incompressible fluid proposed by [53] and [54].

$$p = c^2\rho \tag{A.5}$$

where c is the speed of sound in the medium. As long as the flows are limited to low Mach number, and the conditions are almost isothermal, the solution to this set of equations should approximate the incompressible limit.

The sound speed must be chosen carefully to ensure an efficient an accurate solution of a given problem. The value of c must be large enough that the behavior of the corresponding quasi-incompressible fluid is sufficiently close to that of the real fluid, but it should not be so large to make the time step prohibitively small. According to [55] the Mach number, obtained by the reference velocity and the sound speed, should be 0.1 or less.

A.0.3. Equations in generalized coordinates

Although a Cartesian grid is preferred due to the simplicity and efficiency, in Large Eddy Simulation (LES) methodology the generation of a high-quality resolution in the normal near-wall region is a requirement. In this sense, the use of Cartesian grids can result in a high computational inefficiency as the refinement is extended to regions of the flow in which it is not needed, or even to solid regions. The present model has been developed for use in a generalized curvilinear system allowing a wide range of complex geometries to be modeled efficiently on structured grids.

The coordinates are defined by the transformation $x_i = x_i(\xi_i)$, $j = 1, 2, 3$ through a Jacobian matrix J, which transforms a complex geometry in the Cartesian coordinate system x_i (such as a non-uniform grid or a curvilinear geometry) in the physical space, into a simple orthogonal geometry with uniform grid in the generalized coordinate system (ξ_i) in the computational space. After the transformation, the equations can be solved more easily.

Every term in the inverse Jacobian matrix ($[J_{-1}]$) is expressed as an analytical function of the metrics $\partial x_i/\partial \xi_j$. In this case, the metrics were computed and calculated by the first order internal scheme, and the matrix ($[J]$) is directly computed from $[J_{-1}]$ (see [68] for further details). In consequence, Eq. (A.1) may be rewritten as:

$$\frac{\partial \hat{U}}{\partial t} + \frac{\partial \hat{F}}{\partial \xi_1} + \frac{\partial \hat{F}}{\partial \xi_1} + \frac{\partial \hat{F}}{\partial \xi_1} = \hat{\mathbf{S}_\mathbf{F}} \tag{A.6}$$

$$\hat{U} = \frac{U}{J} \tag{A.7}$$

$$\begin{aligned}
\hat{F} &= \frac{1}{J}\left[\left(\frac{\partial \xi_1}{\partial x_1}F\right) + \left(\frac{\partial \xi_1}{\partial x_2}G\right) + \left(\frac{\partial \xi_1}{\partial x_3}H\right)\right] \\
\hat{G} &= \frac{1}{J}\left[\left(\frac{\partial \xi_2}{\partial x_1}F\right) + \left(\frac{\partial \xi_2}{\partial x_2}G\right) + \left(\frac{\partial \xi_2}{\partial x_3}H\right)\right] \\
\hat{H} &= \frac{1}{J}\left[\left(\frac{\partial \xi_3}{\partial x_1}F\right) + \left(\frac{\partial \xi_3}{\partial x_2}G\right) + \left(\frac{\partial \xi_3}{\partial x_3}H\right)\right]
\end{aligned} \tag{A.8}$$

$$\hat{\mathbf{S}_\mathbf{F}} = \frac{1}{J}\mathbf{S_F} \tag{A.9}$$

where J represents the determinant of the matrix $[J]$ and U is a function of the Cartesian coordinates and time.

A.0.4. Numerical Scheme

The system in generalized coordinates was solved by means of an extension of the fully explicit McCormack scheme, being second order in time and fourth order in space, as devised by [56]. The explicit MacCormack scheme is essentially a predictor-corrector scheme.

The three-dimensional, generalized formulation is shown below:

Predictor

$$\begin{aligned}
U^1_{i,j,k} &= U^n_{i,j,k} \\
&- J^P_{i,j,k}\frac{\Delta t}{\Delta \xi_1}\left[\frac{7}{6}\left(\hat{F}^n_{i+1,j,k} - \hat{F}^n_{i,j,k}\right) - \frac{1}{6}\left(\hat{F}^n_{i+2,j,k} - \hat{F}^n_{i+1,j,k}\right)\right] \\
&+ \frac{\Delta t}{\Delta \xi_2}\left[\frac{7}{6}\left(\hat{G}^n_{i+1,j,k} - \hat{G}^n_{i,j,k}\right) - \frac{1}{6}\left(\hat{G}^n_{i+2,j,k} - \hat{G}^n_{i+1,j,k}\right)\right] \\
&+ \frac{\Delta t}{\Delta \xi_3}\left[\frac{7}{6}\left(\hat{H}^n_{i+1,j,k} - \hat{H}^n_{i,j,k}\right) - \frac{1}{6}\left(\hat{H}^n_{i+2,j,k} - \hat{H}^n_{i+1,j,k}\right)\right]
\end{aligned} \tag{A.10}$$

Corrector

$$\begin{aligned} U^{n+1}_{i,j,k} &= \frac{1}{2}\left[U^{1}_{i,j,k} + U^{n}_{i,j,k}\right] \\ &- \frac{1}{2}J^{C}_{i,j,k}\frac{\Delta t}{\Delta \xi_1}\left[\frac{7}{6}\left(\hat{F}^{1}_{i,j,k} - \hat{F}^{1}_{i-1,j,k}\right) - \frac{1}{6}\left(\hat{F}^{1}_{i-1,j,k} - \hat{F}^{1}_{i-2,j,k}\right)\right] \\ &+ \frac{\Delta t}{\Delta \xi_2}\left[\frac{7}{6}\left(\hat{G}^{1}_{i,j,k} - \hat{G}^{1}_{i-1,j,k}\right) - \frac{1}{6}\left(\hat{G}^{1}_{i-1,j,k} - \hat{G}^{1}_{i-2,j,k}\right)\right] \\ &+ \frac{\Delta t}{\Delta \xi_3}\left[\frac{7}{6}\left(\hat{H}^{1}_{i,j,k} - \hat{G}^{1}_{i-1,j,k}\right) - \frac{1}{6}\left(\hat{H}^{1}_{i-1,j,k} - \hat{H}^{1}_{i-2,j,k}\right)\right] \end{aligned} \tag{A.11}$$

J^P and J^C are the determinants obtained from the Jacobian matrix, computed with the forward and backward schemes, respectively. Moreover (Likewise), interior derivatives in the fluxes as well as diffusive terms are obtained by a central scheme.

A.0.5. Sub-grid Scale Model

A detailed explanation of LES formalism and numerical schemes used in the present work, and an extended validation of the computational code have been presented in [?]

Concerning with the simulations of turbulent flows, we use a Large Eddy Simulation algorith, through the estimation of Subgrid Stress τ_{ij}. In this study, the Selective Structure Function (SSF) model reported by [57] is used. With this model, the Sub Grid Stress is expressed as:

$$\tau_{ij} = \overline{\rho}\nu_t\tilde{S}_{ij} \tag{A.12}$$

Hence, equation (A.3) is replaced by

$$\bar{F}_i = \begin{pmatrix} \bar{\rho}\tilde{u}_i \\ \overline{\rho}\tilde{u}_i\tilde{u}_1 + \bar{p}\delta_{i1} - \tau_{ij} - 2(\overline{\mu} + \overline{\rho}\nu_t)\tilde{S}_{i1} \\ \overline{\rho}\tilde{u}_i\tilde{u}_2 + \bar{p}\delta_{i2} - \tau_{ij} - 2(\overline{\mu} + \overline{\rho}\nu_t)\tilde{S}_{i2} \\ \overline{\rho}\tilde{u}_i\tilde{u}_3 + \bar{p}\delta_{i3} - \tau_{ij} - 2(\overline{\mu} + \overline{\rho}\nu_t)\tilde{S}_{i3} \end{pmatrix} \tag{A.13}$$

where ν_t is the viscosity coefficient for the SGS model. This is given by:

$$\nu_t(\vec{x}, \Delta, t) = C_{sf}\Delta\sqrt{\tilde{F}_2(\vec{x}, \Delta, t)} \tag{A.14}$$

where C_{sf} is a constant and it is related to Kolmogorov's constant C_k through $C_{sf} = 0.105C^{3/2}$. In particular, C_{sf} was taken as 0.104 for $C_k = 1.0$ and $\tilde{F}_2(\vec{x}, \Delta, t)$ represents the second-order velocity structure function, constructed with the filtered instantaneous velocity field. Additionally, $\tilde{F}_2(\vec{x}, \Delta, t)$ depends on the average value from the six adjacent points. $\Delta = (\Delta x \Delta y \Delta z)^{1/3}$ is the filter with.

In the SSF model the eddy viscosity is switched off when the flow is not three-dimensional enough. At a given time, the angle between the vorticity vector at a given grid point and the arithmetic mean of vorticity vectors at the six closest neighboring points is measured. If this angle exceeds 20^o, the eddy viscosity is turned on. Otherwise, only the molecular viscosity is active. This model allows good results to be obtained for various incompressible and compressible turbulent flows. [58]

A.0.6. Vortex identification

The Q criterion is based on a decomposition of the velocity gradient:

$$\nabla v = \mathrm{S_{ij}} + \mathbf{\Omega_{ij}} \tag{A.15}$$

where $S_{ij} = \frac{1}{2}\left(\frac{u_i}{x_j} + \frac{u_j}{x_i}\right)$ is the rate of strain tensor and $\Omega_{ij} = \frac{1}{2}\left(\frac{u_i}{x_j} - \frac{u_j}{x_i}\right)$ is the vorticity tensor, which are the symmetric and antisymmetric components of ∇v. While Ω assesses vortical activity, the strain tensor S measures the amount of stretching and folding which drives mixing to occur. The second invariant of this tensor:

$$Q = \frac{1}{2}\left(\Omega_{ij}\Omega_{ij} - S_{ij}S_{ij}\right) \tag{A.16}$$

Q represents the local balance between shear strain rate and vorticity magnitude, defining vortices as areas where the vorticity magnitude is greater than the magnitude of rate-of-strain , i.e $Q > 0$.

A.1. Interface capturing method

A.1.1. Classical Level-Set methodology

The transport equation of the level set function can be described by the following equation:

This method introduced by [22] is based on the use of a smooth function to describe the interface between two phases.

Let $\phi(x,t)$ denote the LS function with positive value in phase 1 and negative value in phase 2. Therefore, the interface $\Gamma(t)$ is represented by the zero LS of ϕ.

$$\Gamma(t) = \{x \mid \phi(x,t) = 0\} \tag{A.17}$$

The initial value of ϕ is defined as the signed distance between any point of the domain and the interface $\Gamma(t)$. That is,

$$\phi(x,0) = \pm d \tag{A.18}$$

The LS function is advected by the fluid velocity. Solving a convection equation determines the evolution of the interface in a given velocity field u.

$$\frac{\partial \phi}{\partial t} + u \cdot \nabla \phi = 0 \tag{A.19}$$

Important geometric properties on the interface, such as the normal vector n and curvature k, can be obtained easily from LS function through the use of derivative operators.

$$n = \frac{\nabla \phi}{\mid \nabla \phi \mid} \tag{A.20}$$

$$k = \nabla \cdot \left(\frac{\nabla \phi}{\mid \nabla \phi \mid} \right) \tag{A.21}$$

Although the LS function is initialized as a distance function, as the flow field evolves, high velocity gradients can produce wide spreading and/or stretching of the LS function, and no longer remain as a distance function. Unfortunately this requirement is crucial in order to maintain the thickness of the interface constant in time.

A.1.2. Reinitialization

With the intention of keeping ϕ as the signed distance function throughout the time evolution, a reinitialization procedure is performed, based on reinitialization approach of [44]. We replace the $\phi(t, x)$ by another function $d(x)$ (Distance function that just is function of the space) that has the same zero level, but $\mid \nabla d(x) \mid = 1$. The distance function is obtained by solving the following pseudo-transient Hamilton-Jacobi equation:

$$\frac{\partial \phi}{\partial t} + S(\phi_0)(\mid \nabla \phi \mid -1) = 0 \tag{A.22}$$

Eq. A.22 is solved to steady state in pseudo-time τ, with initial condition

$$d(x, \tau = 0) = \phi_0 \tag{A.23}$$

where $S(d)$ is the sign function defined as:

$$S = \frac{d}{\sqrt{d^2 + |\nabla d|^2 \Delta x^2}} \tag{A.24}$$

In the present work, as well as to the LS equation, Eq. A.22 is discretized using the fifth order WENO scheme in space and third order TVD-RK in time. It is important to use higher-order numerical schemes to minimize numerical errors. It is not necessary to perform reinitialitation at every time step. In this work we performed it every 10 to 20 time steps.

A.1.3. Ghost Fluid Method

The GFM offers a way to capture fluid interfaces, avoiding large unphysical oscillations and reducing the numerical smearing of discontinuous variables. As indicate in Fig.(**??**) The idea of the GFM is to introduce two sets of variables, for each separate phase modeled. The governing equation for each field are solved independently and zero level set separates real and ghost zones. Consequently, the task is implementing the GFM method for populating the field variables in the ghost zones of each fluid during each time step.

For smooth well-behaved problems, the method proposed in [47] is the most appropriate. In this approach, in the ghost fluid regions, discontinuous variables across a fluid interface are given using a one-sided extrapolation, and continuous variables are copied from the real fluid on a node by node basis.On the contrary, for large density differences across an interface, i.e., when when density ratio is about 1000:1, [46] suggested an alternative way to constructing the ghost fluid states.

In the modified GFM for air-water interaction, the velocity in the ghost-fluid region for the water and the pressure in the ghost-fluid region for the air are extrapolated from

their real fluid regions, respectively, while the pressure in the ghost-fluid region for the water and the velocity in the ghost-fluid region for the air are copied from their real fluid regions, respectively.

In this paper the modified GFM developed by [46] is used. This same approach has been used successfully by [60] and [52] for simulations of multiphase flows with large density ratio.

A.1.4. Local LS method

The local LS method computations are restricted to a narrow band in the neighborhood of the interface. Only a small fraction of the LS function is considered and updated in every time step. When the interface moves out of the narrow band, the calculation is stopped and a new band is built with the interface at the center of the band. The computational cost is reduced because a significant smaller amount of values have to be updated at every time step. In this work, the approximation of [44] is adopted.

Narrow bands of different size are constructed and updated following the moving interface. The size of the bands is fixed and their values γ_i's are multiple of grid sizes. In general, only two bands are required, but if the motion of the interface involves sensitive quantities such as derivatives of curvature is necessary to used a third narrower band. In this computation three bands γ_1, γ_2 and γ_3, around the interface are considered, where $0 < \gamma_1 < \gamma_2 < \gamma_3$.

The choice of the width γ_i's depends of the stencils of the schemes used to spatial discretization. The widest stencil used in this computation is the fifth-order WENO scheme. So the values chosen are: $\gamma_1 = 1.5\Delta l$, $\gamma_2 = 3\Delta l$ and $\gamma_3 = 6\Delta l$, for instance, where Δl is the average space step size ($\Delta l = \sqrt{\Delta x^2 + \Delta y^2 + \Delta z^2}$).

The main idea in the local LS method consists of two components. The first one is to update the level set function only in the band of width γ_3 in the neighborhood of the zero LS according with the following equation,

$$\frac{\partial \phi}{\partial t} + c(\phi) u \cdot \nabla \phi = 0 \tag{A.25}$$

where $c(\phi)$ is a cut-off function that modified the motion and is expressed by

$$c(\phi) = \begin{cases} 1 & \text{if } \mid \phi \mid \leq \gamma_2 \\ \frac{(\mid\phi\mid-\gamma_3)^2(2\mid\phi\mid+\gamma_3-3\gamma_2)}{(\gamma_3-\gamma_2)^3} & \text{if } \gamma_2 < \mid \phi \mid \leq \gamma_3 \\ 0 & \text{if } \mid \phi \mid > \gamma_3 \end{cases} \tag{A.26}$$

The cutoff function is introduced to prevent numerical oscillations at the band boundary and prevent discontinuities.

The second step in the local LS method requires to update the computational band as the interfaces evolves in time. Since we have already regularized the evolution using the reinitialization equation (A.22), the signed distance value of the LS function can be used to determine the computational band at the next time step. So this step requires no extra computational cost.

A.2. Volume of Fluid Method

The volume of fluid method was introduced by [21] and, since its conception has been widely used in several works. In VOF method, the computational domain is divided into small cells. Each cell is assigned a discontinuous concentration function χ representing the volume fraction of one of the fluids within the cell. From these cell fractions, the position of the interface can be determined using an interface reconstruction procedure within each cell that is intersected by the interface.

The characteristic function χ with a value between zero and one is advected according to:

$$\frac{\partial \chi}{\partial t} + u \cdot \nabla \chi = 0 \tag{A.27}$$

Because the function is a conservative variable, the method conserve mass exactly. However, despite the accurately mass - conserving properties of the method, the interface

reconstruction and the approximations on geometric properties of the interface are computationally expensive, especially in three dimensional simulations.

A.2.1. Mass Conserving Method

The MCLS method was developed by [35]. This method is based on the idea of mass conservation improving through the use of a explicit function f that directly relates the VOF function to the LS function and its gradient as:

$$\psi = f(\phi, \nabla\phi) \tag{A.28}$$

To conserve mass, corrections are applied to the LS function ϕ using the VOF function ψ. This is achieve by application of three steps:

- Calculation of VOF function from LS function ($\psi^n = f(\phi^n, \nabla\phi^n)$)
- Advection of VOF function (ψ^{n+1})
- Correction of function ϕ^{n+1} with the advected VOF function ψ^{n+1}, such that $\phi^{n+1} = f(\phi^{n+1}, \nabla\phi^{n+1})$

The three steps are explained in detail below

Step 1

The VOF function ψ in a computational cell in terms of LS function ϕ is defined as:

$$\psi(x_k) = \frac{1}{vol(\Omega_k)} \int H(\phi) d\Omega \tag{A.29}$$

where Ω_k is a cell in the grid, x_k correspond to the center node of Ω_k and H is a Heaviside step function. LS function ϕ is linearized around x_k, which leads to:

$$\varphi = \phi_k + \nabla\phi_k \cdot (x - x_k), \tag{A.30}$$

Where $\nabla\phi_k$ is approximated by central differences. The volume fraction ψ_k cut from cell Ω_k by the plane defined by $\varphi = 0$ is computed mapping onto a unit cube Ω with coordinates $(\xi, \eta, \zeta)\epsilon(-1, 1)^3$ (Fig. (**??**)). The Eq. (A.30) can be rewritten as:

$$\varphi = \phi_k + D_\xi\xi + D_\eta\eta + D_\zeta\zeta \tag{A.31}$$

where

$$\begin{aligned} \xi &= (x - x_k)/\Delta x \\ \eta &= (y - y_k)/\Delta y \\ \zeta &= (z - z_k)/\Delta z \end{aligned} \tag{A.32}$$

Conducive to numbering possible interface topologies in the cube the axes are chosen such that:

$$D_\xi \geq D_\eta \geq D_\zeta \geq 0 \tag{A.33}$$

where

$$\begin{aligned} D_\xi &= max(\mid D_x \mid, \mid D_y \mid, \mid D_z \mid) \\ D_\zeta &= min(\mid D_x \mid, \mid D_y \mid, \mid D_z \mid) \\ D_\eta &= \mid D_x \mid + \mid D_y \mid + \mid D_z \mid - D_\xi - D_\zeta \end{aligned} \tag{A.34}$$

and

$$\begin{aligned} D_x &= \Delta x \frac{\partial \phi}{\partial x} \mid_k \\ D_y &= \Delta y \frac{\partial \phi}{\partial y} \mid_k \\ D_z &= \Delta z \frac{\partial \phi}{\partial z} \mid_k \end{aligned} \tag{A.35}$$

The VOF function is derived geometrically by computing the relative volume enclosed by the cut plane within Ω_k defined by the zero level set of the linearized LS function.

After some mathematical manipulations function f is computed geometrically from the volume cut out from the cube. Function f is evaluated as:

$$f = \begin{cases} \dfrac{A}{6 D_\xi D_\eta D_\zeta} & \phi \leq 0 \\ 1 - f(-\phi, \nabla\phi) & \phi > 0 \end{cases} \tag{A.36}$$

where

$$\begin{aligned} A &= \max\left(\Phi_A, 0\right)^3 - \max\left(\Phi_B, 0\right)^3 - \max\left(\Phi_C, 0\right)^3 \\ &- \max\left(\Phi_D, 0\right)^3 + \max\left(\Phi_E, 0\right)^3 \end{aligned} \tag{A.37}$$

and

$$\begin{aligned}
\Phi_A &= \Phi_k + \frac{1}{2}D_\xi + \frac{1}{2}D_\eta + \frac{1}{2}D_\zeta \\
\Phi_B &= \Phi_k + \frac{1}{2}D_\xi + \frac{1}{2}D_\eta - \frac{1}{2}D_\zeta \\
\Phi_C &= \Phi_k + \frac{1}{2}D_\xi - \frac{1}{2}D_\eta + \frac{1}{2}D_\zeta \\
\Phi_D &= \Phi_k - \frac{1}{2}D_\xi + \frac{1}{2}D_\eta + \frac{1}{2}D_\zeta \\
\Phi_E &= \Phi_k + \frac{1}{2}D_\xi - \frac{1}{2}D_\eta - \frac{1}{2}D_\zeta
\end{aligned} \tag{A.38}$$

Φ_A represents the value $\Phi(x_A)$ at corner A, and similarly for the other corners.

Step 2

In the present work, like the LS equation and reinitialization equation, the VOF function is advanced by using a using the fifth order WENO scheme in space and third order TVD-RK in time.

Step 3

The LS function ϕ^{n+1} is corrected with the VOF function ψ^{n+1}, such as

$$\mid f(\phi_k^{n+1}, \nabla\phi_k^{n+1}) - \psi_k^{n+1} \mid < \epsilon \tag{A.39}$$

where ϵ is some tolerance. A solution ϕ is found trough an iteration method: method leaves ϕ unmodified in a grid point when the VOF constraint is satisfied and it makes corrections locally when this constraint is not satisfied. This is achieved by using the inverse function g of f as given in Eqn. (A.36) with respect to argument ω_k:

$$f(g(\psi, \nabla\phi), \nabla\phi) = \psi \tag{A.40}$$

This equation is solved by means of Secant method iterations. This procedure improve mass conserving.

A.3. Discretization of the VOF and LS equations

So as to treat correctly the evolution of the LS function according to Eq. (A.19) numerical schemes should have enough accuracy. In this work, the third-order Runge-Kutta TVD scheme by [49] is employed for time discretization; whereas for space discretization, we apply the fifth order WENO scheme proposed by [44].

A.3.1. Spacial Discretization

In this work, the fifth-order accurate WENO scheme [48] is adopted. This approximation is based in the fact that Hamilton-Jacobi equations are closely related to conservations laws. WENO scheme takes a convex combination of the three fluxes:

$$\phi_x^1 = \frac{a}{3} - \frac{7b}{6} + \frac{11c}{6} \tag{A.41}$$

$$\phi_x^2 = -\frac{b}{6} + \frac{5c}{6} + \frac{d}{3} \tag{A.42}$$

$$\phi_x^3 = \frac{c}{3} + \frac{5d}{6} - \frac{e}{6} \tag{A.43}$$

If any of the three approximations interpolates across a discontinuity, it takes a minimal weight in the convex combination in order to minimize its contribution. Otherwise, in smooth regions of the flow, all three approximations are allowed to make a significant contribution in a way that improves the local accuracy from third order to fifth order.

The physical fluxes are splitted through the local Lax-Friedrichs flux splitting method. Designating ϕ_x^- and ϕ_x^+ respectively, the numerical fluxes obtained from the positive and negative splitting.

For ϕ_x^- the stencil in equations (A.41 to A.43) are defined by: $a = \frac{\phi_{i-2}-\phi_{i-3}}{\Delta x}$, $b = \frac{\phi_{i-1}-\phi_{i-2}}{\Delta x}$, $c = \frac{\phi_i-\phi_{i-1}}{\Delta x}$, $d = \frac{\phi_{i+1}-\phi_i}{\Delta x}$ and $e = \frac{\phi_{i+2}-\phi_{i+1}}{\Delta x}$.

The WENO ϕ_x^- approximation is given by:

$$\phi_x = \omega_1\phi_x^1 + \omega_2\phi_x^2 + \omega_3\phi_x^3 \tag{A.44}$$

The weights, ω_k, are defined as:

$$\omega_1 = \frac{\alpha_1}{\alpha_1 + \alpha_2 + \alpha_3} \tag{A.45}$$

$$\omega_2 = \frac{\alpha_2}{\alpha_1 + \alpha_2 + \alpha_3} \tag{A.46}$$

$$\omega_3 = \frac{\alpha_3}{\alpha_1 + \alpha_2 + \alpha_3} \tag{A.47}$$

where $\omega_1 + \omega_2 + \omega_3 = 1$ and α_k, are defined as:

$$\alpha_1 = \frac{1}{(\epsilon + S_1)^2} \tag{A.48}$$

$$\alpha_2 = \frac{6}{(\epsilon + S_2)^2} \tag{A.49}$$

$$\alpha_3 = \frac{3}{(\epsilon + S_3)^2} \tag{A.50}$$

and the smoothness of the stencils S_k, are defined as:

$$S_1 = \frac{13}{12}(a - 2b + c)^2 + \frac{1}{4}(a - 4b + 3c)^2 \tag{A.51}$$

$$S_2 = \frac{13}{12}(b - 2c + d)^2 + \frac{1}{4}(b - d)^2 \tag{A.52}$$

$$S_3 = \frac{13}{12}(c - 2d + e)^2 + \frac{1}{4}(3c - 4d + e)^2 \tag{A.53}$$

where ϵ is a small number, around $O(10^{-6})$.

The weights values for high order accuracy, the optimal fifth order, in smooth regions are: $\omega_1 = 0.1$, $\omega_2 = 0.6$ and $\omega_3 = 0.3$., respectively.

The function ϕ_x^+ is constructed with the stencils: $a = \frac{\phi_{i+3} - \phi_{i+2}}{\Delta x}$, $b = \frac{\phi_{i+2} - \phi_{i+1}}{\Delta x}$, $c = \frac{\phi_{i+1} - \phi_i}{\Delta x}$, $d = \frac{\phi_i - \phi_{i-1}}{\Delta x}$ and $e = \frac{\phi_{i-1} - \phi_{i-2}}{\Delta x}$ and using equations (A.41), (A.42), (A.43) as approximations to ϕ_x^+. The weights are given by equations (A.45), (A.46) and (A.47).

A.3.2. Temporal Discretization

The third order TVD Runge-Kutta method is given by,

$$\begin{cases} \phi^1 = \phi^n + \Delta t L(\phi^n) \\ \phi^2 = \frac{3}{4}\phi^n + \frac{1}{4}(\phi^1 + \Delta t L(\phi^1)) \\ \phi^{n+1} = \frac{1}{3}\phi^n + \frac{2}{3}(\phi^2 + \Delta t L(\phi^2)) \end{cases} \tag{A.54}$$

The third order TVD method is generally recommended, since it has the greatest accuracy and largest time step stability region of the TVD schemes. By cause of its large stability region for a sufficiently small time step, it is guaranteed to be linearly stable for a variety of problems.

Bibliography

[1] C. Galvin, J. Geophys. Res. **73**, 3651 (1968).

[2] F. Grasso, B. Castelle, and B. Ruessink, Cont. Shelf. Res. **43**, 133 (2012).

[3] A. Pedrozo-Acuña, A. R. de Alegría-Arzaburu, A. Torres-Freyermuth, E. Mendoza, and R. Silva, Coast. Eng. **58**, 722 (2011).

[4] L. Dianyong, M. Yuxiang, D. Guohai, and P. Marc., Eur. J. Mech. B-Fluid **52**, 206 (2015).

[5] S. Brown, D. Greaves, V. Magarand, and D. Conley, Coast. Eng. **114**, 177 (2016).

[6] W. J. Pringle, N. Yoneyama, and N. Mori, Coast. Eng. **114**, 99 (2016).

[7] Z. Xie, Appl. Math. Model. **37**, 3698 (2013).

[8] Y. Watanabe and H. Saeki, Coast. Eng. J. **41**, 281 (1999).

[9] E. D. Christensen and R. Deigaard, Coast. Eng. **42**, 53 (2001).

[10] P. Lubin, S. Vincent, S. Abadie, and J. P. Caltagirone, Coast. Eng. **53**, 631 (2006).

[11] K. Nadaoka, M. Hino, and Y. Koyano, J. Fluid Mech. **204**, 359 (1989).

[12] F. Ting and J. Kirby, Coast. Eng. **24**, 51 (1994).

[13] F. Ting, Coast. Eng. **53**, 441 (2006).

[14] F. Ting, Coast. Eng. **55**, 522 (2008).

[15] Y. Watanabe, H. Saeki, and R. J. Hosking, J. Fluid Mech. **545**, 291 (2005).

[16] E. D. Christensen, Coast. Eng. **53**, 463 (2006).

[17] P. Lubin and S. Glockner, Coast. Eng. Proc. **33** (2012).

[18] P. K. Stansby, A. Chegini, and T. C. D. Barnes, J. Fluid Mech. **374**, 407 (1998).

[19] I. M. Janosi, D. Jan, K. G. Szabo, and T. Tel, Exp. Fluids. **37**, 219 (2004).

[20] T. O'Donoghue, D. Pokrajac, and L. Hondebrink, Coast. Eng. **57**, 513 (2010).

[21] C. Hirt and B. Nichols, J. Comput. Phys. **39**, 201 (1981).

[22] S. Osher and J. A. Sethian, J. Comput. Phys. **79**, 12 (1988).

[23] E. Olsson and G. Kreiss, J. Comput. Phys. **210**, 225 (2005).

[24] E. Olsson, G. Kreiss, and S. Zahedia, J. Comput. Phys. **225**, 785 (2007).

[25] O. Desjardins, V. Moureau, and H. Pitsch, J. Comput. Phys. **227**, 8395 (2008).

[26] L. Zhao *et al.*, Comput. Fluids **100**, 138 (2014).

[27] M. J. Berger and J. Oliger, J. Comput. Phys. **53**, 484 (1984).

[28] M. Sussman *et al.*, J. Comput. Phys. **148**, 81 (1999).

[29] R. Nourgaliev and T. Theofanous, J. Comput. Phys. **224**, 836 (2007).

[30] H. Kim and M.-S. Liou, Comput. Fluids **44**, 111 (2011).

[31] M.-H. Chung, Comput. Fluids **71**, 469 (2013).

[32] M. Sussman and E. G. Puckett, J. Comput. Phys. **162**, 301 (2000).

[33] D. Sun and W. Tao, Int. J. Heat Mass Transf. **53**, 645 (2010).

[34] X. Lv, Q. Zoua, Y. Zhaob, and D. Reevea, J. Comput. Phys **229**, 2573 (2010).

[35] S. P. van der Pijl, A. Segal, and C. V. andP., Int. J. Numer. Meth. Fluids **47**, 339 (2005).

[36] Z. Wang, J. Yang, B. Koo, and F. Stern, Int. J. Multiphas Flow **35**, 227 (2009).

[37] Y. Wang, S. Simakhina, and M. Sussman, J. Comput. Phys. **231**, 6438 (2012).

[38] Q. Li, J. Ouyang, B. Yang, and X. Li, Appl. Math. Model. **36**, 2262 (2012).

[39] X. Lv, Q. Zou, and D. Reeve, Adv. Water Resour. **34**, 1320 (2011).

[40] B. Leonard, Comput Methods Appl Mech Eng. **81**, 17 (1991).

[41] T. Wang, H. Li, Y. Feng, and D. Shi, Int. J. Heat Mass Transfer. **67**, 70 (2013).

[42] J. A. Sethian, *A Fast Marching Level Set Method for Monotonically Advancing*

Fronts (PROC. NAT. ACAD. SCI, 1995).

[43] M. Sussman, P. Smereka, and S. Osher, J. Comput. Phys. **114**, 146 (1994).

[44] D. Peng, B. Merriman, S. Osher, H. Zhao, and M. Kang, J. Comput. Phys. **155**, 410 (1999).

[45] D. Adalsteinsson and J. A. Sethian, J. Comput. Phys. **118**, 269 (1995).

[46] R. P. Fedkiw, J. Comput. Phys. **175**, 200 (2000).

[47] R. P. .Fedkiw, T. Aslam, B. Merriman, and S. Osher, J. Comput. Phys. **152**, 457 (1999).

[48] G. Jiang and D. Peng, SIAM J. Sci. Comput. **21**, 2126 (1999).

[49] R. P. Fedkiw, B. Merriman, R. Donat, and S. Osher, The penultimate scheme for systems of conservation laws: Finite difference eno with marquina's flux splitting, in *with Marquina's Flux Splitting, Progress in Numerical Solutions of Partial Differental Equations, Arachon*, 1998.

[50] M. Salinas-Vazquez and O. Metais, Journal of Fluid Mechanics **453**, 201 (2002).

[51] A. J. Chorin, J. Comput. Phys. **135**, 118 (1997).

[52] R. Nourgaliev, T. Dinh, and T. Theofanousi, Int. J. Multiphase Flow. **30**, 901 (2004).

[53] A. Perrin and H. Hu, J. Comput. Phys. **212**, 166 (2006).

[54] J. P. Morris, P. J. Fox, and Y. Zhu, J. Comput. Phys. **136**, 214 (1997).

[55] J. Monaghan, J. Comput. Phys. **110**, 399 (1994).

[56] D. Gottlieb and E. Turkel, Math. Comput. **30**, 703 (1976).

[57] E. David, *Modelisation of compressible and hypersonic flows: an instationary approach*, PhD thesis, Grenoble Institute of Technology, 1993.

[58] M. Salinas-Vázquez *et al.*, Appl. Math. Model. **37**, 9132 (2013).

[59] M. Salinas-Vázquez, M. de la Lama, W. Vicente, and E. Martínez, Appl. Math. Model. **35**, 4393 (2011).

[60] H. Terashima and G. Tryggvason, J. Comput. Phys. **228**, 4012 (2009).

[61] Center for Turbulence Research Report No., , 1988 (unpublished).

[62] L. Lobovsky, E. B.-V. ad F. Castellana, J. Mas-Soler, and A. Souto-Iglesias, J. FLuid Struct. **48**, 407 (2014).

[63] K. Kleefsman, G. Fekken, A. Veldman, B. Iwanowski, and B. Buchner, J. Comput. Phys. **206**, 363 (2005).

[64] A. Ritter*Die Fortpflanzung der Wasserwellen* Vol. 36 (Vereine Deutcher Ingenieure Zeitswchrift, 1892).

[65] J. Cubos-Ramírez *et al.*, Computer and Fluids **136**, 212 (2016).

[66] J. Stoker, *Water waves: the mathematical theory with applications* (Interscience Publishers, 1957).

[67] Z. Zhou, J. Sangermano, T.-J. Hsu, and F. C. K. Ting, J. Geophys. Res. Oceans **119** (2014).

[68] C. A. J. Fletcher, *Computational techniques for fluid dynamics. 1. , Fundamental and general techniques*Springer series in computational physics (Springer-Verlag, Berlin, Paris, 1991).

List of figures

List of tables